

UNIVERSITY OF TARTU
FACULTY OF SCIENCE AND TECHNOLOGY
INSTITUTE OF CHEMISTRY
INSTITUTE OF PHYSICS

Kerda Keevend

**MICROWAVE-HYDROTHERMAL SYNTHESIS OF WATER-DISPERSIBLE
LUMINESCENT NANOPARTICLES OF YTTRIUM PHOSPHATES AND
FLUORIDES DOPED WITH Nd³⁺ ION**

Master's thesis (30 ECTS points)

Supervisors: Alexander Vanetsev, PhD

Yury Orlovskiy, Dr. hab, PhD

TARTU 2015

Contents

1. Introduction.....	3
2. Literature overview.....	4
2.1. Luminescent nanoparticles of rare-earth compounds and their biomedical applications.....	4
2.2. Soft chemical routes for the synthesis of luminescent nanoparticles.....	7
2.2.1. High temperature solvolysis	7
2.2.2. Co-precipitation from the aqueous solution.....	8
2.2.3. Microemulsion method	9
2.2.4. Hydrothermal synthesis	10
2.3. Microwave hydrothermal synthesis	11
3. Experimental section.....	13
3.1. Synthesis of nanoparticles.....	13
3.1.1. Synthesis of yttrium orthophosphates nanoparticles.....	13
3.1.2. Synthesis of potassium-yttrium fluorides nanoparticles	13
3.2. Measurement techniques	14
3.2.1. X-Ray diffraction (XRD) analysis	14
3.2.2. Infrared spectroscopy (IR) measurements	14
3.2.3. Transmission electron microscopy (TEM)	14
3.2.4. Thermogravimetric (TG) measurements.....	15
3.2.5. Dynamic light scattering analysis (DLS).....	15
3.2.6. Fluorescence spectroscopy.....	15
3.2.7. Fluorescence kinetics spectroscopy	15
4. Results and discussions.....	16
4.1. YPO ₄ nanoparticles	16
4.1.1. Phase composition of as prepared samples	16
4.1.2. Morphology and thermal behaviours of the synthesized nanoparticles.....	18
4.2. KYF ₄ and KY ₃ F ₁₀ nanoparticles	23
4.2.1. Phase composition of as prepared samples	23
4.2.2. Morphology and thermal behaviour of the synthesized nanoparticles	25
4.3. Spectroscopic studies of synthesized nanoparticles	29
Acknowledgements.....	36
5. Conclusions.....	37
6. Mikrolaine hüdrotermaalse meetodiga sünteesitud vees dispergeeritavad luminesseerivad neodüümiga dopeeritud ütrium fosfaadi ja fluoriidi nanoosakesed.....	39
7. References.....	41

1. Introduction

Despite the rapid development of medicine the survival rate of cancer has not improved for the past 30 years [1]. Hence, a development of an advanced method of cancer treatment, especially non-invasive, which minimizes the disturbance of already weakened organs and systems, is a crucial task. Nowadays, the combination of nanotechnology and biomedicine is leading to faster diagnostics and provides new approaches to non-invasive treatment. For example, laser-induced fluorescence diagnostics is suitable for medical use as an imaging technique. There are several prospective candidates for bio-imaging agents; including rare-earth (RE) doped nanoparticles (NP), quantum dots, organic dyes etc. [2] Among them rare-earth doped nanoparticles with fluorescence emission in near infrared (NIR) region are especially promising, as biological tissues have so-called “transparency window” in this range and it is possible to create agents for in-vivo bio-imaging with deep penetration (7-10 mm) into human body. [2, 3, 4] Other advantages of rare earth ions include narrow spectral lines and submillisecond lifetimes of the emitting metastable levels [2].

However, in aqueous media the fluorescence of rare earth ions in NIR region is substantially quenched [5]. Mainly, this fluorescence quenching is induced by vibrations of –OH molecular groups that are easily attached to the surface of NPs and mesopores inside of them or exist in the volume of NPs in the form of structural defects. [6, 7, 8] This is a fundamental obstacle, as most of the synthesis methods of water dispersible nanoparticles are carried out either in water or in other –OH containing media. Also, the concentration of nanoparticles in a colloidal solution during *in vivo* experiments should be as low as possible to avoid or at least minimize intoxication [9]. Moreover, the imaging itself is conducted in water media (human body). Thus, the elaboration of synthetic techniques allowing minimizing the water content in nanoparticles and, therefore, reduce fluorescence quenching, while preserving good dispersability in water, is a very important task from the practical point of view.

The aim of this work is to develop synthesis method of water-dispersible luminescent nanoparticles of yttrium phosphates and fluorides doped with Nd³⁺ ions using microwave hydrothermal treatment of freshly precipitated gels, as well as a study the luminescent properties of obtained nanoparticles in order to estimate their applicability as bioimaging agents.

2. Literature overview

2.1. Luminescent nanoparticles of rare-earth compounds and their biomedical applications

Nowadays nanotechnology and nanoparticles are very well known and much studied, because nanoparticles exhibit properties different from that of bulk materials [10]. Despite the fact that nanoparticles are already investigated in many fields, like electronics [11], biomedicine [12], optics [13], and chemical synthesis [14], the exact definition about nanoparticles is not yet settled. Most often particles with the size between 1 and 100 nm are called nanoparticles.

Although the diagnostic procedures have developed rapidly, the survival rate of cancer has not significantly improved over the past 30 years [1]. Combining nanotechnology with biomedicine opens perspectives of faster diagnostics, less harmful treatment and more localized imaging of pathological cells [15]. By all means, not all nanoparticles are suitable for biomedical applications. Desired nanoparticles are biocompatible, small, have narrow size-distribution, and they should be easily dispersible in water. It is shown, that the nanoparticles for bioimaging should have size around 50 nm. [16, 17] Unfortunately, the toxicity studies do not develop as fast as synthesis and functionalization of nanoparticles, which makes their everyday use impossible for now [10].

In general, nanoparticles for biomedical applications are divided into five large categories: metallic, magnetic, semiconductor, luminescent and composite nanoparticles [18]. Each category has its own most widely known examples. Gold and silver nanoparticles are the most interesting subjects in case of metallic nanoparticles. Many researchers have developed gold nanoparticles as drug carriers [19] or as sensors [20]. Iron oxide magnetic nanoparticles are widely investigated for MRI contrast enhancement agents [21].

Rare-earth doped nanoparticles have several advantages over traditional organic phosphors and quantum dots and now they are the most attractive candidates for imaging applications [2, 22]. The trivalent rare-earth ions have narrow spectral lines and submillisecond lifetimes of the emitting metastable levels, which allow employing time-resolved fluorescence spectroscopy thus crucially enhancing the signal-to-noise ratio. Furthermore, they are uniquely photostable and moreover, it is possible to use them in bioimaging, because they have deep tissue penetration (7-10mm) [2, 3, 4]. The group of rare-earth elements contains lanthanum and 14 lanthanides, scandium, and yttrium. Lanthanide ions have intra-4f and 4f-

5d transitions, which give them sharp fluorescence emission, and make them valuable material for luminescent phosphors. Doping host matrix with emissive Ln^{3+} ion is very effective because the size and chemical properties of lanthanide ions are similar. The luminescence can be divided into two main categories: up-conversion (UC) and down-conversion (DC) emission process. [3]

Rare-earth containing up-converting nanoparticles are the most known for possible biomedical applications. In UC process a photon with higher energy is emitted after the absorption of two or more lower energy excitation photons. This process has drawn a lot of attention recently, because it is a successful method generating visible light from near infra-red light. Up-conversion processes can be divided into three main categories: excited state absorption (ESA), energy transfer up-conversion (ETU) and photon avalanche (PA). Up to date, ETU has been the most used method, because PA shows slow response and the results depend on pump power, while ESA is the least efficient method. [3]

Up-conversion luminescence is realized when the inorganic matrix (host), activated Ln^{3+} ion (activator) and sensitizer obey to certain criteria. Ideal host material has low lattice phonon energy to ensure the maximum radiative emission. Right now, fluorides are the most common host materials for up-conversion nanoparticles, because they have low phonon energies ($\sim 500 \text{ cm}^{-1}$) and they are chemically stable. Chemical stability is a problem for other halides, because they are hygroscopic and their use is limited, although they have lower phonon energies (less than 300 cm^{-1}). The most common host for up-conversion nanoparticles is NaYF_4 . Dopants, also called as activators, generate up-conversion emission. The most commonly used activators are Er^{3+} , Tm^{3+} and Ho^{3+} ions, because of their ladder-like energy levels. The concentration of dopant is usually low, so there would be less energy losses. The optimal dopant concentration (C_{opt}) is the concentration at which the photoluminescence intensity has a maximum value. Usually, the system is co-doped with another lanthanide ion to enhance the up-conversion emission, called sensitizer. Most commonly used sensitizer is Yb^{3+} ion. [3, 23]

In the DC process, the photons with higher energy are converted into lower energy photons. The down-conversion luminescence system contains also a host matrix and activated Ln^{3+} ions. The matrix acts as a host crystal for keeping the Ln^{3+} ions tightly and also sensitize their luminescence. Several inorganic compounds are suitable for being DCL host material, like RE oxide, oxysulfide, fluoride, phosphate and vanadate. Most commonly used activators for visible light are Eu^{3+} , Tb^{3+} , Sm^{3+} and Dy^{3+} . In this case, the dopant concentration is also kept

rather low to avoid concentration quenching of luminescence and distortion of the host crystal structure. Photoluminescence intensity depends also on the host material, particles size, calcination temperature and synthesis conditions. Though the most commonly used dopant-ions for down-converting nanoparticles are emitting in visible range, there is a substantial amount of research dedicated to the nanoparticles doped with ions emitting in near infra-red region. [3] Such nanoparticles have attracted recently a lot of attention as potential materials for bioimaging and theranostics applications, as biological tissues become partially transparent in this spectra range, so-called biological tissues transparency window. [17]

Figure 1 shows the transmittance spectrum of a typical human tissue (according to absorption and scattering spectra). There are two main biological windows, which are determined by taking into account two aspects: absorption of different compounds found from human tissue (like water and haemoglobin) and the scattering caused by the tissue. [17]

1. The first biological window stretches from 700 nm to 980 nm. This area lies between the visible absorption band of haemoglobin and the characteristic 980 nm absorption band of water. In this region, the absorption has greatly vanished, but scattering still exists. The relevance of scattering decreases in longer wavelengths. [17]
2. The second biological window is from 1000 nm to 1400 nm, which lies in between water absorption bands. As mentioned before, the relevance of scattering decreases in longer wavelengths, so in this spectra range, optical scattering is minimal. On the other hand, optical absorption has not completely vanished. [17]

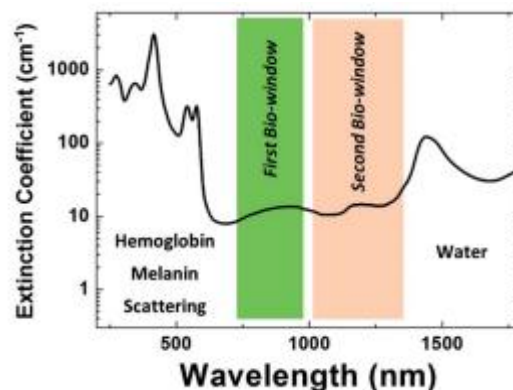


Figure 1. The transparency windows of biological tissues [17].

Only few ions have high absorption cross-section in the spectral range of interest. The most suitable candidates are Nd^{3+} and Tm^{3+} ions. The main problem in the near IR range is the fluorescence quenching, including self-quenching, which does not allow to achieve high

fluorescence quantum yield in these ions. [6, 7, 24] Fluorescence quantum yield (η) is defined as a ratio of photons absorbed by a fluorophore to those emitted via fluorescence. Current parameter is difficult to determine and several different methods are currently used, like absolute and relative methods (see more in ref. [3]). In the transparency window, the fluorescence quenching is induced by the vibrations of –OH molecular groups, which are easily attached to the surface of a nanoparticle and can quench fluorescent donors in the thin surface layer of the NP. Another possibility is that they are present in the volume of obtained particles, for example in the mesopores, and can quench the main part of donors in the volume of the NP. Since most of the studies with luminescent nanoparticles are related to the up-conversion nanoparticles, the problem of fluorescence quenching is not raised properly. Most of the up-conversion nanoparticles emit light in the visible or even in the UV light, where the quenching by –OH molecular groups is not an issue. [3, 25] On the other hand, for the down-converting nanoparticles this problem is crucial, therefore the development of advanced synthetic techniques, which allows minimizing the -OH-induced fluorescence quenching in the water-dispersible nanoparticles, is vital and important task from the practical point of view.

2.2. Soft chemical routes for the synthesis of luminescent nanoparticles

2.2.1. High temperature solvolysis

Among all the soft chemical synthetic routes, high temperature solvolysis is one of the most popular and used method for synthesizing dispersible nanoparticles. Solvothermal route involves dissolving organic precursors in high-boiling organic solvent together with surfactants and other host matrix materials and heating the solution up to the temperatures at which solvolysis of dissolved materials leads to formation of desired compound in the form of nanoparticles. The precursors are sometimes inorganic, but usually organic acid salts, for example trifluoroacetate [22], oleate [26] or acetate [27]. The media is usually oleic acid [22, 26], noncoordinating octadecene [22] or a mixture of high-boiling organic solvents [22]. Oleic acid and oleylamine polar groups both act as a surfactant, playing two different roles in the mixture: 1) capping the surface of the nanoparticles to ensure their dispersibility in organic solvents and prevent the aggregation and 2) the selective absorption effect is controlling the growth of the nanoparticles. [3] The concentration of oleic acid in the mixture influences the size of the nanoparticles. Smaller concentration of oleic acid leads to bigger nanoparticles. [26]

Current method gives monodispersed, crystalline, well-defined and phase-pure nanoparticles. It is suitable for synthesizing small nanoparticles, with mean size around 10 nm. Also, it is possible to further functionalize nanoparticles. [3, 28] There are several parameters which influence the morphology, size and crystal phase of synthesized nanoparticles including temperature, pressure, surfactant, precursor composition, heating rate, cooling rate, reaction time, solvent and concentration of the reagents. However, high temperature solvolysis has some drawbacks; the synthesis conditions are rather harsh (high temperature, waterless, oxygen-free and inert gas protection), it has high-cost, toxic precursors are present in the reaction mixture and it gives hazardous by-products. [29]

Zou et al synthesized luminescent nanoparticles in ethylene glycol using polyethylenimine as a surfactant. The group obtained cubic $\text{NaYF}_4:\text{Yb}^{3+}/\text{Er}^{3+}$ nanoparticles with good crystallinity. The average size of synthesized particles was 34 nm. [30] Using surfactants makes the surface of obtained nanoparticles hydrophobic, because the polar head of surfactant is targeted towards the surface of nanoparticles and hydrophobic tail is addressed towards solvent. This makes particles hard to disperse in hydrophilic media and gives great drawback in subsequent biological functionalization. To avoid this drawback Bogdan et al synthesized ligand-free $\text{NaYF}_4:\text{Er}^{3+},\text{Yb}^{3+}$ up-converting nanoparticles using a modified solvolysis technique and obtained nanoparticles with a mean size around 25 nm. The oleate ligand was removed from synthesized nanoparticles using post-treatment with acid. By this way, the pH of the solution is changing; causing the protonation of the oleate ligand and oleic acid is released. Ligand-free nanoparticles dispersed in water show higher up-conversion luminescence compared to oleate-capped nanoparticles. A study in different pH values showed that reducing the pH results in positive zeta potential, which proposes that the surface of oleate-free nanoparticles is protonated [LnOH_2^+], enhancing the red emission. Also further functionalization with biomolecules is possible for imaging and detection applications in biological applications. [31]

2.2.2. Co-precipitation from the aqueous solution

Co-precipitation method is probably one of the simplest methods that are used for the synthesis of nanoparticles. Nanoparticles are obtained when two or more solutions, containing reagents, are mixed together in desired proportions under stirring. During this process, cation(s) and anion(s) form insoluble salt in the reaction mixture, which precipitates. Reaction can be conducted at the room temperature or at elevated temperatures. Elevated

temperatures might be needed to obtain more crystalline particles. [16] This method is user-friendly, inexpensive, and environmentally green, has simple protocols, uses low-cost equipment and does not produce so many toxic by-products compared to the solvothermal method [3, 28]. The size and the shape of synthesized nanoparticles depend on numerous factors, like solvent, pH of the solution, used surfactant, ratio between ions, ionic strength and the nature of initial salts (perchlorates, chlorides, sulphates and nitrates). [16, 32, 33]

However, it is rather difficult to obtain nanoparticles with narrow size distribution, as it is hard to control the kinetic factors. In order to control the size distribution of synthesized nanoparticles, it is important to keep nucleation process and growth process apart from each other, which is almost impossible in case of the co-precipitation technique. [16] Aubry *et al.* synthesized luminescent CaF₂ NPs doped with Yb³⁺ ion using the co-precipitation method. They obtained particles with a mean size around 24 nm and with asymmetric size distribution. The surface of the synthesized particles was covered with the –OH groups. Annealing removed the residues of nitrates. The excitation spectrum was collected at 980 nm and revealed the presence of Er³⁺ and Tm³⁺ ions, although they were not used as doping ions. Energy transfer from the sensitizer to the additional acceptors took place, causing up-conversion process. The radiative relaxation resulted in green and blue emission. The chemical analysis revealed impurities in the initial ytterbium nitrate salt, which was used as a precursor. [34]

2.2.3. Microemulsion method

The traditional microemulsion is two-phased inverse micelle (water-in-oil) system, which contains water phase, surfactant and oil phase. Surfactant is stabilizing the water droplets in the oil phase, so it results in a transparent solution. Water phase contains dissolved reactants. After mixing two microemulsions, water droplets collide and coalesce. This creates nanoreactors for the synthesis of nanoparticles. The size of the nanoparticles depends on the size of the water droplet. The size of the droplet is changeable by varying the water-to-surfactant molar ratio (W_0). Generally, increasing the value of W_0 gives larger particles. [21] The mixture is usually further treated, using ultrasonication [21] or thermal treatment [35] to obtain well crystalline particles.

Microemulsion method has proved to be suitable method for the synthesis of nanoparticles. It has several advantages, for example it is easy to prepare it, because they form spontaneously at room temperature. The small size of water droplets in the oil allows synthesizing small

particles. However, the formation of microemulsion requires huge amount of surfactants, which can be irritating. Although the microemulsion is thermodynamically stable, many factors including temperature and pH affect its stability. The yield of this method is rather low, which makes it not user-friendly. [3, 36]

Several water-surfactant-oil systems have been used to synthesize luminescent nanoparticles: water-TX-100-cyclohexane [21], water-Brij-97-cyclohexane [21], water-Igepal CO-520-*n*-heptane [21], water-CTAB-isooctane [37] and water-CTAB-*n*-hexane [37]. Mai et al prepared luminescent CaWO₄ and ZnWO₄ nanoparticles doped with Tb³⁺ and Eu³⁺ ions. For the synthesis, current group used cyclohexane-surfactant-1-hexanol mixture, wherein non-ionic (Triton X-100) and cationic (CTAB) surfactants were added to the reaction mixtures. Freshly synthesized nanoparticles were crystalline. Unfortunately, the luminescence properties did not show good results. For that reason, further treatment with autoclave was used. Post-treated particles showed intense luminescence under UV-radiation. The size and shape of nanoparticles depend on the synthesized matrices and used surfactant. For CaWO₄ matrix and CTAB nearly spherical nanoparticles with a mean size around 50 nm were obtained. Meanwhile, synthesis with Triton X-100 gave broader size distribution and irregular shape for NPs. For ZnWO₄ matrix, synthesis with Triton X-100 gave larger nanoparticles with a mean size around 80 nm. For the CTAB-based synthesis, obtained nanoparticles were rod-shaped with a length of 80-150 nm. CaWO₄ and ZnWO₄ exhibit blue emission, but doping with lanthanide ions widens the emission spectrum from blue (non-doped) to green (Tb³⁺, maxima at 546 nm) and red (Eu³⁺ maxima at 614 nm). This gives a full-colour emission with using only one host matrix. [35]

2.2.4. Hydrothermal synthesis

Hydrothermal synthesis is widely used to synthesize nanoparticles. In hydrothermal synthesis water is used as a solvent in elevated temperatures and pressures above its boiling point. This increases the solubility of inorganic compounds, which usually are poorly soluble in ambient conditions. To obtain desired synthesis conditions, it is necessary to use a closed high-pressure vessel (autoclave). [3]

The term „hydrothermal“ has an geological origin. British geologist Sir Roderick Murchison (1792–1871) was the first person to use this method for describing action of water at elevated temperature and pressure in the Earth’s crust, which leads to the formation to different rocks and minerals. [38] Also, hydrothermal synthesis was used to grow single crystals. The

synthesis of single crystals is using the fact that the solution has temperature gradient between opposite ends of autoclave. In the hotter end, nutrient is dissolved in the solvent. Due to the temperature gradient between two areas, the nutrient, which dissolves in hotter area, but not in lower temperature, deposits on the seed of the crystal, which causes the growth of crystal. [39] The area of applications became wider and other types of materials, such as micro-and nanocrystalline powders [40], micro-and mesoporous materials [41], glass-ceramic composites [42] were synthesized using this method.

Hydrothermal synthesis is used as a one-step synthesis method. Typically a reaction mixture contains precursor, water and organic additive. The precursors are usually salts containing rare-earth elements, like chlorides [40] and nitrates [43]. Organic additive (surfactant) can tune the morphology of nanoparticles due to the selective adsorption on the different facets of nanocrystals. [3] The tuning of the morphology of nanoparticles can be achieved by organic-additive free [40, 43], hydrophilic-ligand-assisted [44] and hydrophobic-ligand-assisted [45] synthesis. Wang et al developed a simple method for synthesizing nanomaterials by hydrothermal synthesis. It is based on a liquid-solid-solution (LSS) process. In the mixture, three phases exist: sodium linoleate (solid), the mixture of ethanol and linoleic acid (liquid) and water/ethanol solution containing the metal ions (solution). Phase-transfer and separation mechanism occur at the interfaces of the liquid, solid and solution phases during the synthesis, resulting in nanoparticles with hydrophobic layer, which precipitate due to the weight of synthesized nanoparticles, the incompatibility between hydrophobic surface of obtained nanoparticles and their hydrophilic surrounding. [46]

Hydrothermal synthesis has several advantages compared to the other methods, including rather green chemistry route because of water-based synthesis, easily controllable reaction conditions, narrow size distribution, relatively low cost and high yield. This method is suitable for the synthesis of nanoparticles, because it gives monodispersed and highly homogeneous particles. The main disadvantage of current method is a long reaction time and to overcome this drawback it is possible to use microwave treatment, which intensifies diffusion and crystallization processes comparing to conventional heating. [3, 29, 47]

2.3. Microwave hydrothermal synthesis

Microwave hydrothermal synthesis route is very similar to conventional hydrothermal synthesis. The source of cation is usually a salt, either chloride [48] or nitrate [7].

Microwaves can influence organic [49] and inorganic [6, 7] reactions. The main advantage using microwaves in chemical reactions is the uniform heating of the mixture [50] and the shorter synthesis time [51]. Conventional heating is slow and not efficient method, because it depends on the thermal conductivity of different materials, including the autoclave. Very often, the temperature in the vessel is higher than in the solution. Since molecules under microwave irradiation start to produce internal heat, the mixture heats up faster. [50] Microwave hydrothermal synthesis is also a green route, because for most of the times, water is used as a solvent [52]. Other advantages include high yield [49] and scalability [49].

Ryabochkina et al. studied YPO_4 nanoparticles doped with Er^{3+} ion as possible drug delivery systems. Nanoparticles were synthesized using microwave hydrothermal synthesis. Two different systems were obtained: $\text{Y}_{0.95}\text{Er}_{0.05}\text{PO}_4$ (sample 1) and $\text{Y}_{0.95}\text{Er}_{0.05}\text{PO}_4 \cdot 0.8\text{H}_2\text{O}$ (sample 2). The first sample showed xenotime-type structure, while the second sample exhibited rhabdophane-type hydrate of yttrium orthophosphate. TEM analysis confirmed that the Sample 1 has almost isotropic particles, while the Sample 2 has mostly elongated, ellipsoidal nanoparticles. While the XRD measurements suggested the size of nanocrystals for the Sample 1 to be around 19 nm and for the Sample 2 around 15 nm, the TEM micrographs revealed the size of the crystals to be 37 nm and 30 nm, for the Sample 1 and the Sample 2 respectively. The luminescence emission spectra of $\text{Y}_{0.95}\text{Er}_{0.05}\text{PO}_4$ and $\text{Y}_{0.95}\text{Er}_{0.05}\text{PO}_4 \cdot 0.8\text{H}_2\text{O}$ show the emission in IR range, which make their use in biomedical application more probable due to the transparency window. [53]

As shown, there are several wet chemistry methods for synthesizing nanoparticles for biomedical applications. However, finding the method, which gives small, monodispersed and well-crystalline nanoparticles with reasonable time, cost and effort is rather difficult. For the past decade, much effort has been placed in developing up-converting nanoparticles, which have a light emission in the visible spectrum range. The main problem with these particles is the low quantum yield and the emission in the visible range, which does not transmit human tissues. For that reason, nanoparticles, which emit in the transparency window, have high quantum yield and make diagnostics local, are desirable. This work will focus on synthesizing water-dispersible luminescent nanoparticles, using three different matrices and Nd^{3+} ion as a luminescent ion, which has an emission in 850-1300 nm spectral range [54].

3. Experimental section

3.1. Synthesis of nanoparticles

The initial reagents used in the synthesis without any further purification include $\text{Nd}(\text{NO}_3)_3 \cdot 5\text{H}_2\text{O}$ (Aldrich, 99.999% purity), $\text{Y}(\text{NO}_3)_3 \cdot 4\text{H}_2\text{O}$ (Aldrich, 99.999% purity), $\text{K}_2\text{HPO}_4 \cdot 3\text{H}_2\text{O}$ (Aldrich, 99.9% purity), KF (Aldrich, >99% purity), KOH (KhimMed, >99% purity) and deuterium oxide (Aldrich 99.9% purity).

Syntheses are carried out using the Speedwave Four (Berghof GmbH, Germany) laboratory device (2.45 GHz, 1kW maximum output power). All the centrifugations are carried out using Thermo Scientific Heraeus Multifuge X1 device with Fiberlite F15-6x100y rotor.

3.1.1. Synthesis of yttrium orthophosphates nanoparticles

For the synthesis of YPO_4 nanoparticles doped with Nd^{3+} ion (1% and 0.1% mass percent), $\text{Y}(\text{NO}_3)_3 \cdot 4\text{H}_2\text{O}$ (4.950 mmol or 4.995 mmol, respectively) and $\text{Nd}(\text{NO}_3)_3 \cdot 5\text{H}_2\text{O}$ (0.050 mmol or 0.005 mmol) are dissolved in 10 ml of deionized water. The solution of rare-earth salts is added dropwise to the 5, 10, 25 or 50 mmol $\text{K}_2\text{HPO}_4 \cdot 3\text{H}_2\text{O}$ solution under vigorous stirring. The measured natural pH of $\text{K}_2\text{HPO}_4 \cdot 3\text{H}_2\text{O}$ solution is 9.3. The pH is adjusted using 0.1M KOH solution up to 10.3, 11.3, and 13.6. After that, the freshly precipitated gel is stirring for additional 15 minutes. The freshly precipitated gel is further diluted with 10 ml of deionized water and transferred to the 100 ml Teflon autoclave. The autoclave is placed under microwave irradiation for 1, 2 and 4 hours at 200 °C. The resulting solution is cooled, centrifuged and washed several times with deionized water. The resulting powder was dried in air at 100 °C overnight.

To reduce fluorescence quenching we annealed samples at high temperatures: one of the samples of $\text{YPO}_4:\text{Nd}^{3+}$ (0.1%) nanoparticles is annealed at 900 °C for 1 hour.

3.1.2. Synthesis of potassium-yttrium fluorides nanoparticles

For the synthesis of KYF_4 and KY_3F_{10} nanoparticles doped with Nd^{3+} ion (0.1% mass percent), $\text{Y}(\text{NO}_3)_3 \cdot 4\text{H}_2\text{O}$ (4.994 mmol) and $\text{Nd}(\text{NO}_3)_3 \cdot 5\text{H}_2\text{O}$ (0.005 mmol) are dissolved in 10 ml of deionized water. The solution of rare-earth salts is added dropwise to the 5 mmol or 50 mmol $\text{KF} \cdot 2\text{H}_2\text{O}$ solution under vigorous stirring. To improve the redispersibility of obtained nanoparticles, a biocompatible surfactant Emuksol-268 (NIOPIK) is added to the solution. Surfactant is added to the system in two different stages: early in the stage to nitrate

solutions and after the formation of gel. The freshly precipitated gel was diluted with 10 ml of deionized water and left under stirring for 15 minutes. The solution is transferred to the 100 ml Teflon autoclave and placed under the microwave irradiation for 4 hours at 200 °C. The resulting solution is cooled, centrifuged and washed several times with deionized water. The resulting powder is dried in air at 100 °C overnight. To reduce the fluorescence quenching, synthesis in deuterium oxide is conducted with the same synthesis route. After drying the samples, they are stored in desiccator.

3.2. Measurement techniques

3.2.1. X-Ray diffraction (XRD) analysis

The X-ray diffraction analysis on synthesized nanoparticles is performed using the D/MAX 2500 and SmartLab diffractometers (Rigaku™, CuK_α-radiation). Nanoparticles are measured in the powdered form. X-ray data analysis (peak detection, fitting and crystallite size determination) are performed using updated version of AXES program [55]. The peaks are identified using JCPDS database and the literature data [56]. Instrumental broadening of the reflections are measured on the bases of standard material SRM-660 (LaB6). Physical broadening (β) of reflections is calculated by using Voigt decomposition method. Apparent volume weighted X-ray crystallite size $\langle D \rangle_v$ in the direction normal to observed atomic planes is estimated using Scherrer equation:

$$D = \frac{\lambda}{\beta \cos \theta} \quad (1)$$

where λ is the wavelength of X-ray irradiation and θ is the Bragg angle for the particular reflection studied.

3.2.2. Infrared spectroscopy (IR) measurements

Infrared absorption spectra are measured using Perkin Elmer Spectrum GX FT/IR spectrometer. Spectra are measured in the powder form.

3.2.3. Transmission electron microscopy (TEM)

The morphology of obtained nanoparticles is measured by the means of TEM using Leo912 AB Omega electron microscope at 100kV accelerating voltage. The samples are prepared using Hielscher UP200S ultrasonic processor (Germany, for stand use, 200 watts, frequency 24kHz). 1 mg of obtained nanoparticles is dispersed in ethanol using the aid of

ultrasonication tip for 5 minutes. The resulting colloid is placed on TEM copper grid and let it dry for several hours.

3.2.4. Thermogravimetric (TG) measurements

The thermogravimetric analysis (TGA) for the powdered samples is performed using the LABSYS avo 1600 thermoanalyser coupled by a heated transfer line to the Pfeiffer mass spectrometer for the analysis of effluent gases.

3.2.5. Dynamic light scattering analysis (DLS)

The dynamic light scattering analysis is performed using Photocor Complex spectrometer. For the measurements, water colloid is prepared with a low concentration (0.1 mg/ml) using the aid of Bandelin SONOPLUS HD2070 ultrasonication device with a submersible waveguide KE76 for 1 minute. For the preparation of the water colloid, 1 mg of synthesized nanoparticles is dispersed in 1 ml of water with the aid of ultrasonication for 1 minute (using the CT-400D, CTBRAND ultrasonication bath). After that 0.1 ml of obtained colloid is mixed with 0.9 ml Proxanol 268 (NIOPIK) solution (0.01 mass percent) using intensive ultrasonication (Bandelin SONOPLUS HD2070 with a submersible waveguide KE76) for 1 minute.

3.2.6. Fluorescence spectroscopy

The fluorescence emission spectra measurements for the $\text{YPO}_4:\text{Nd}^{3+}$ nanoparticles are conducted at room temperature. For the $\text{KYF}_4:\text{Nd}^{3+}$ NPs and for the $\text{KY}_3\text{F}_{10}:\text{Nd}^{3+}$ nanoparticles measurements are conducted at room temperature and 10 K using the HORIBA Fluoromax-4 spectrofluorometer.

3.2.7. Fluorescence kinetics spectroscopy

The fluorescence spectra and kinetics are measured in near-infrared spectral range using pulsed laser excitation from the optical parametric oscillator (OPO) Ekspla NT342/1/UVE ($t_p=15$ ns, $f = 20$ Hz). The fluorescence is dispersed by a MDR-23 monochromator (LOMO) and detected by a photomultiplier Pheu-79 and a multi-channel analyser (Fast Comtec P7882) with 100 ns time resolution using the photon counting technique. The edge-filter BLP-785R (Semrock) is attached to the front slit of the monochromator to prevent the entry of scattering light of the laser excitation into the MDR-23 monochromator.

4. Results and discussions

4.1. YPO₄ nanoparticles

4.1.1. Phase composition of as prepared samples

Our first task was to study the influence of the duration of synthesis, the ratio between yttrium and phosphate ion in initial solution and the pH of the initial solution to the morphology, size and luminescent properties of obtained nanoparticles. As a result, we found that depending on the synthesis conditions, obtained YPO₄ nanoparticles were either tetragonal xenotime-type yttrium orthophosphate (YPO₄) or the hexagonal rhabdophane-type hydrate of yttrium orthophosphate (YPO₄·0.8 H₂O) or the mixture of both (Table 1).

Table 1. Phase composition of as-prepared samples according to the results of XRD analysis.

Sample	Duration of synthesis, h	Y ³⁺ :PO ₄ ³⁻ ratio	pH	Phase composition, according to XRD data
D-1	1	1:1	natural (9.3)	YPO ₄
D-2	2	1:1	natural (9.3)	YPO ₄
D-4	4	1:1	natural (9.3)	YPO ₄
R-2	2	1:2	natural (9.3)	Mixture of YPO ₄ and YPO ₄ ·0.8H ₂ O
R-5	2	1:5	natural (9.3)	YPO ₄ ·0.8H ₂ O (+ small amount of YPO ₄)
R-10	2	1:10	natural (9.3)	YPO ₄ ·0.8H ₂ O (+ small amount of YPO ₄)
pH-10	2	1:1	10.3	YPO ₄
pH-11	2	1:1	11.3	YPO ₄ ·0.8H ₂ O (no traces of YPO ₄)
pH-13	2	1:1	13.6	Amorphous halo (+ traces of YPO ₄ ·0.8H ₂ O phase and unidentified secondary phases)

According to the XRD results (Figure 2), as-prepared YPO₄ nanoparticles do not contain any traces of secondary phases and are well-crystalline. The calculated $\langle D \rangle_v$ value for the anhydrous nanoparticles is 20±4 nm. At the same time, the YPO₄·0.8H₂O phase has lower crystallinity and most of synthesized samples contained other phases (like YPO₄ or

unidentified secondary phases). Calculated $\langle D \rangle_v$ value for R-2 sample is 13 ± 3 nm. All the peaks from $\text{YPO}_4 \cdot 0.8\text{H}_2\text{O}$ phase were shifted towards smaller angles compared to the literature data. It can be due to the different synthesis method, which leads to different content of crystalline water.

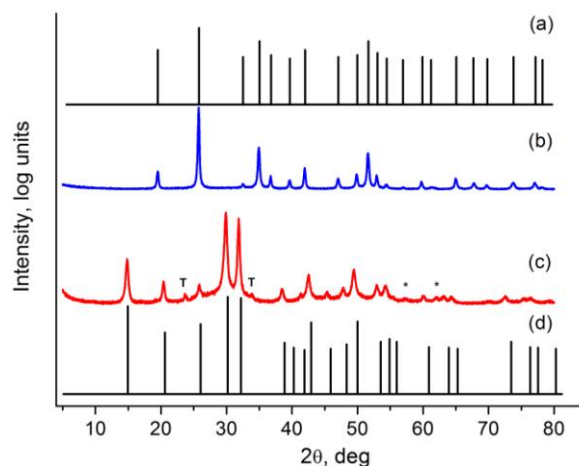


Figure 2. X-ray diffraction patterns of non-calcinated samples; a) the reference data of tetragonal YPO_4 #11-254 from the JCPDS PDF2 database, b) the pattern on D-2 sample, c) the pattern on the R-10 sample, d) the standard pattern of hexagonal $\text{YPO}_4 \cdot 0.8\text{H}_2\text{O}$ phase from the JCPDS PDF2 database; T-traces of tetragonal yttrium orthophosphate phase, *-unidentified secondary phase.

The stoichiometric ratio between Y^{3+} and PO_4^{3-} ions in the starting mixture leads to the formation of tetragonal orthophosphate; results do not depend on the duration of synthesis. The formation of the rhabdophane-type hydrate is more sensitive to the reaction conditions. Hydrate forms when raising the ratio between two ions up to 1:10 or the reaction solution pH above 11. Halo on Figure 2c, shows that the sample synthesized in the excess of PO_4^{3-} ions contains amorphous phase. This allows us to suggest that the formation of the $\text{YPO}_4 \cdot 0.8\text{H}_2\text{O}$ phase is precluded compared to the YPO_4 phase. Although the exact formation mechanism of the $\text{YPO}_4 \cdot 0.8\text{H}_2\text{O}$ phase is unknown, the available data allows suggesting, that the large excess of anion in the reaction mixture creates higher degree of supersaturation and therefore a higher rate of nucleation. As a result, the particles are more aggregated and less crystalline.

The $\text{YPO}_4 \cdot 0.8\text{H}_2\text{O}$ nanoparticles are also obtained using increased pH values (Table 1). The sample is phase pure and does not contain any traces of tetragonal YPO_4 phase, unlike in the case of anion excess. Obtained nanoparticles also show higher degree of crystallinity. However, the high value of pH is not the only force for the formation of the hydrate phase. Hydrate phase is also obtained in the case of natural pH, but with a huge excess of anion.

Synthesized nanoparticles were also studied using Fourier transform infrared spectroscopy (FT-IR). The spectra of the YPO_4 and the $\text{YPO}_4 \cdot 0.8\text{H}_2\text{O}$ phases are shown in Figure 3. As it is seen from the figure, the PO_4^{3-} broad bands around 1000 cm^{-1} look different for two phases. The hydrate phase exhibit more pronounced splitting of this band and also the red shift. Splitting may occur because of significantly different positions of the PO_4^{3-} anions in crystal lattices, since some of them are in close proximity of H_2O molecules in channels and some of them are not. Also, the red shift of 640 cm^{-1} band could have the same nature.

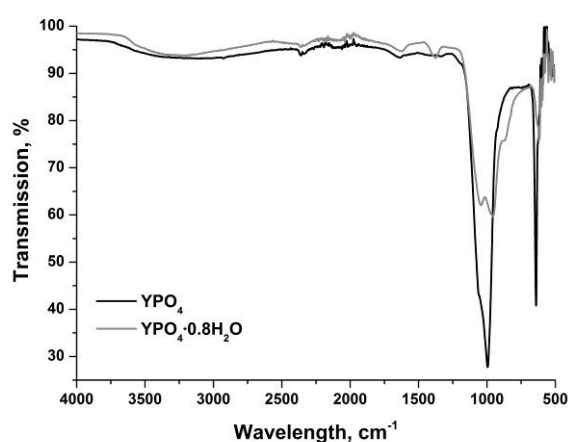


Figure 3. The FT-IR transmission spectra of phosphate nanoparticles.

Although the as-prepared sample should contain significant amount of water, only slightly stronger absorption in the anti-symmetrical stretched vibrational bands (around 3300 cm^{-1}) of the hydroxyl groups is noticed. Nevertheless, the absorption band around 1400 cm^{-1} , which is only notable in the $\text{YPO}_4 \cdot 0.8\text{H}_2\text{O}$ spectrum, may correspond to the vibrations of structurally bound water molecules. It is worth to note, we did not see any strong and sharp absorbance around 3500 cm^{-1} , which is reported previously for the $\text{YPO}_4 \cdot 0.8\text{H}_2\text{O}$ phase [57].

4.1.2. Morphology and thermal behaviours of the synthesized nanoparticles

The comparison of morphology of the YPO_4 nanoparticles synthesized in 200°C with different duration, without the anion excess shows unexpected decrease of the mean size of obtained nanoparticles. The shape of obtained isotropic nanoparticles varies from ellipsoidal to square. The mean sizes of synthesized nanoparticles are $46 \pm 15\text{ nm}$, $41 \pm 12\text{ nm}$ and $34 \pm 13\text{ nm}$ for 1, 2 and 4 hour synthesis, respectively. The decrease of particle size is probably related to the higher crystallinity and the dehydration of the amorphous phase, which is left on the surface and/or in the volume of obtained nanoparticles, because the volume of the hydrated amorphous phase is bigger than for the crystallized samples.

Figure 4 represents the TEM images and size distribution of synthesized nanoparticles. The sample distribution for the particles obtained after one hour treatment is close to normal, but the increase of the treatment durations leads to more lognormal distribution. This most likely indicates that, longer treatment also leads to Ostwald ripening and recrystallization of nanoparticles. From the TEM images it is also seen that all particles contain significant amount of mesopores, which allows suggesting that aggregation is taking place during the formation of nanoparticles.

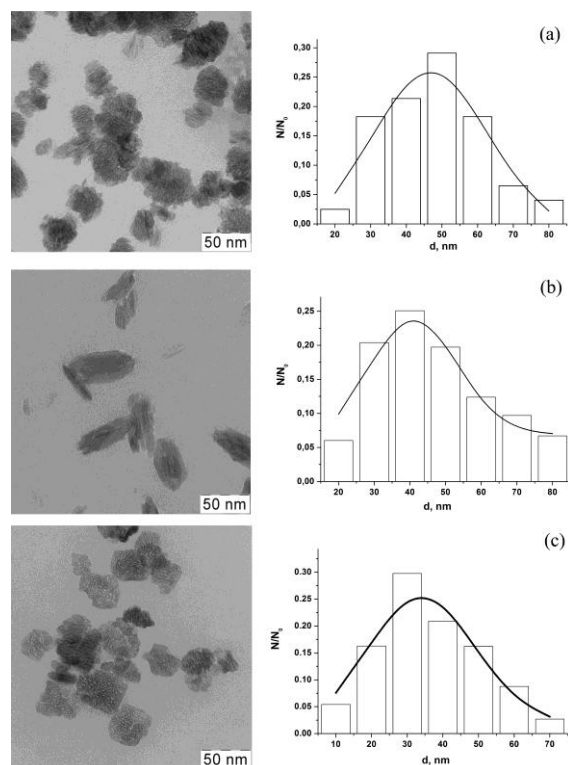


Figure 4. The TEM micrographs of YPO_4 nanoparticles, varying the duration of synthesis: 1 hour, 2 hours and 4 hours, respectively.

The $YPO_4 \cdot 0.8H_2O$ nanoparticles synthesized at natural pH, but using large excess of anions, leads to strongly agglomerated elongated nanoparticles (Figure 5a). According to the TEM data, the mean size of these nanoparticles is around 40 nm, but the XRD data give the coherent scattering range of 18 ± 2 nm. The significant difference between two data is mostly due to the anisotropic shape and low crystallinity of these nanoparticles. It is very probable, that synthesized particles contain several smaller nanocrystallites, which are divided by the layers of the amorphous material.

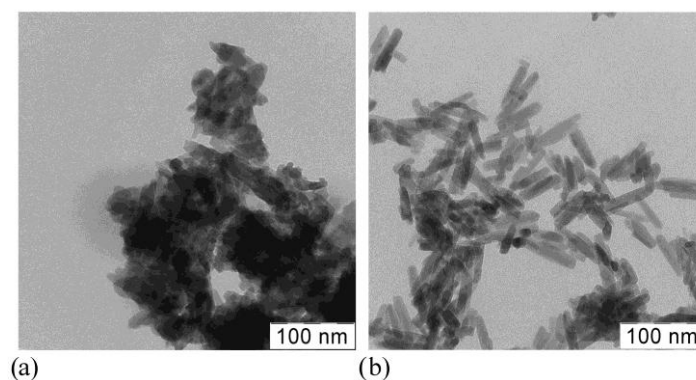


Figure 5. The TEM micrographs of synthesized $\text{YPO}_4 \cdot 0.8\text{H}_2\text{O}$ nanoparticles.

At the same time, nanoparticles synthesized at elevated pH, show well-defined nanorods (**Figure 5b**). It allows suggesting that the mechanism of formation of obtained nanoparticles is different in this case. It seems that in the case of anion excess, there are two competing processes: aggregation of primary nuclei and their growth; while in elevated pH the growth of rod-like nanoparticles dominates. One of the possible explanations is the structure of precipitated gel during these processes. Since the gel is spatially confined structure, the rate of aggregation of primary nuclei and rate of the nucleation can be different. In the case of an excess of PO_4^{3-} ion, the higher rate of nucleation is expected, so the aggregation of nuclei is more intensive and this leads to the formation of shapeless aggregates. In the case of the increased pH, the nucleation process is less intensive, so the growth process is more probable. Specific sorption of OH^- ions on selected facets of growing crystals, which facilitates growth of nanorods, is also known in hydrothermal conditions. One can also notice, that the $\text{YPO}_4 \cdot 0.8\text{H}_2\text{O}$ nanoparticles with defined shape do not contain as many mesopores as the YPO_4 nanoparticles. This can also be related to the growth mechanism, because the formation of pores is improbable during the growth of nanorods.

Our next task was to investigate thermal behaviour of obtained nanoparticles and especially carefully characterize the poorly studied phase transition from the $\text{YPO}_4 \cdot 0.8\text{H}_2\text{O}$ phase to the tetragonal YPO_4 phase.

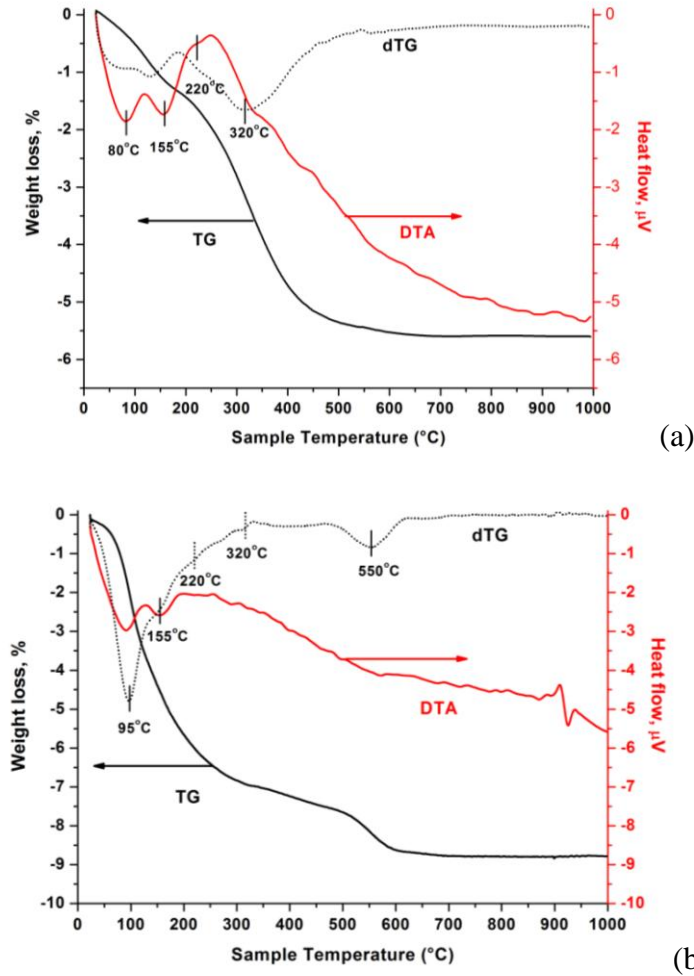


Figure 6. TG/DTG-DTA curves for the YPO₄ (D-2) (a) and YPO₄·0.8H₂O (R-10) (b) phases. Figure 6a represents the TG/DTG-DTA data for the anhydrous YPO₄ phase. On the DTA curve, it is clearly seen four minima, which correspond to the removal of physically adsorbed water molecules and the surface –OH groups. One can observe the first minimum around 80 °C, which responds to leaving of H₂O molecules adsorbed on the outer surface of nanoparticles. The total weight loss is rather small, staying under 1%. The second minimum is observed at 155 °C, which is attributed to the removal of the –OH groups attached to the outer surface of synthesized nanoparticles. From 200 °C to 400 °C one can see two minima, while according to the TG data, the main weight loss occurs. As it is seen on the Figure 4, the YPO₄ nanoparticles contain great amount of mesopores. Probably in this temperature range, mesopores open and the weight loss is related to the removal of the mother solution from the pores, followed by the removal of the –OH groups attached to the surface of pores. Mesopores located close to the surface open at lower temperatures (around 220 °C) and the ones with longer distance from the outer surface open later (they are finally open around 320 °C). Therefore, TG data shows wide temperature range for weight loss, but do not have well-

pronounced steps. This can be due to two reasons: first, there is a continuum of distances from a mesopore to the outer surface of nanoparticle and second, after the mesopore is opened and the mother solution is removed, the -OH groups attached to the surface of the mesopores are removed. For that reason, one cannot distinguish minima from the TG curve very well, because these two processes are continuous and last up to 500 °C or even slightly higher temperature.

The DTA/DTG curves for the $\text{YPO}_4 \cdot 0.8\text{H}_2\text{O}$ phase have in general the same features, although some differences appear (Figure 6b). First of all, the minimum related to the removal of absorbed water on the surface, has shifted to 95 °C and the weight loss is also larger. It can be due to the lower crystallinity; therefore there are more water molecules adsorbed on the surface of nanoparticles, which are more strongly bonded to it. It is previously shown [58] that removal of crystalline water for this phase starts at rather low temperatures ($\sim 100^\circ\text{C}$), so the hydrate also starts to decompose. Again, the TG curve does not have pronounced steps, which can be explained with the continuous removal of crystalline water, which starts slightly above 100°C. According to the previous study [58], this phase is stable up to 500 °C. From the TG curve, it is seen that the weight loss reaches to 8%, so almost all crystalline water is removed in this temperature.

As mentioned before, the weight loss around 200-400 °C in anhydrous phase is related to the opening of mesopores, but in the $\text{YPO}_4 \cdot 0.8\text{H}_2\text{O}$ phase the weight loss in this temperature range is insignificant. Since the mechanism of formation of nanoparticles is different in these two cases, the formation of mesopores is not in favour in hydrate phase.

The TG data shows the weight loss reaches to 8%, so it is possible to suggest that most of the crystalline water molecules are removed. An additional minimum is seen in the DTG curve at 550 °C. This minimum can be related to the phase transition, because the structural transition from the hexagonal phase starts above 500°C [58]. According to the mass-spectroscopy analysis of the effluent gases, this weight loss is also caused by the evaporation of water. Although most of crystalline water is removed from the crystal, the weight loss is still around 1%. This is most likely connected to the removal of the -OH groups or water molecules, which are strongly bonded in the volume of the hydrated phase. One may assume the presence of -OH groups in the structure of the hexagonal orthophosphate requires charge compensation, which is associated with the defects in the cation sublattice, for example, intercalation of K^+ ions into interstitial space. Since the hexagonal crystal structure is stable up to 500 °C, it is probable that the remaining groups are stabilizing it up to this temperature

(Figure 7c). As soon as the removal of these groups begins, also the transformation into the stable tetragonal phase starts. The temperature is relatively low and the diffusion of ions is slow, so this process is kinetically hampered. Annealing hydrate phase up to 700 °C or even higher, leads to the mixture of hexagonal and tetragonal phases (Figure 7b).

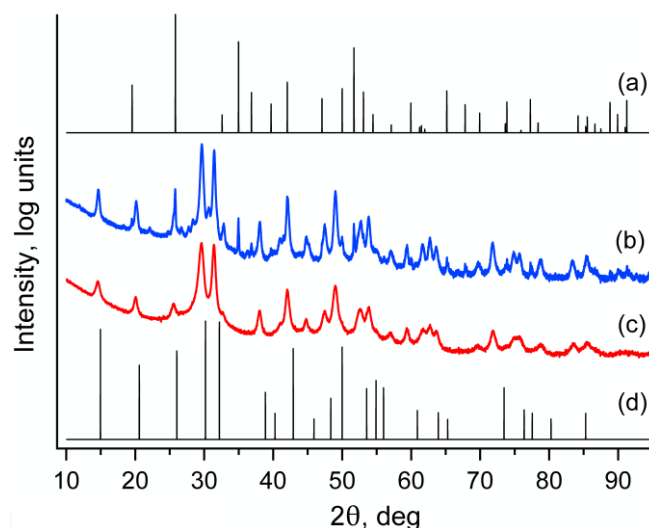


Figure 7. The X-ray diffraction patterns of annealed samples; (a) the standard fingerprint pattern of the tetragonal YPO_4 #11-254 from the JCPDS PDF2 database, (b) the pattern of the $\text{YPO}_4 \cdot 0.8\text{H}_2\text{O}$ (R-10) sample annealed at 700 °C for 10 hours, (c) the pattern of the $\text{YPO}_4 \cdot 0.8\text{H}_2\text{O}$ sample annealed at 470 °C for 10 hours, (d) the standard fingerprint pattern of the hexagonal $\text{YPO}_4 \cdot 0.8\text{H}_2\text{O}$ #42-82 from the JCPDS PDF2 database.

Although annealing nanoparticles at high temperatures leads to the removal of –OH groups on their surface, it also causes the aggregation. The size of nanoparticles used in biomedical application should not exceed 100 nm, so the aggregated samples are not suitable for the usage in biomedical applications.

4.2. KYF_4 and KY_3F_{10} nanoparticles

4.2.1. Phase composition of as prepared samples

We synthesized series of samples varying the ratio between yttrium and fluoride ions in the initial solution. Depending on the synthesis conditions, obtained nanoparticles are either cubic phase of the KYF_4 or the KY_3F_{10} . The modified cubic phase of the KYF_4 is ascribed earlier in the literature and it seems to exist only in the nanostate [56]. The typical pattern of as-prepared KYF_4 nanoparticles is seen in the Figure 8. The XRD data render that obtained nanoparticles are well-crystalline and do not have any traces of secondary phases. The calculated $\langle D \rangle_v$ for the KYF_4 nanoparticles is 36 ± 4 nm, which is remarkably larger than previously discussed YPO_4 nanoparticles. This confirms the better crystallinity of the KYF_4

nanoparticles (Figure 8a). The peaks are a bit shifted compared to the reference data [56]. Since the nanoparticles used in reference have different dopant and its concentration, one can attribute the shift to that.

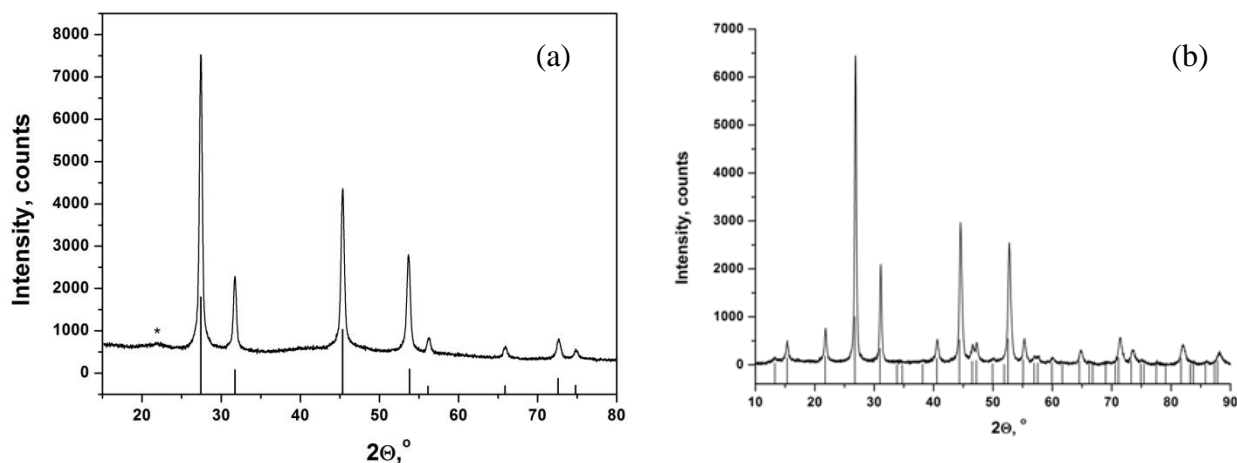


Figure 8. (a) The XRD pattern of as-prepared KYF_4 nanoparticles compared to the reference data [56] and (b) the XRD pattern of as-prepared KY_3F_{10} nanoparticles compared to #01-071-2757 from the JCPDS PDF2 database.

The XRD data for the KY_3F_{10} nanoparticles is shown in the Figure 8b. As one can see, the peaks are also narrow and well-defined, which indicates that synthesized particles are well crystalline and do not contain any traces of secondary phases. The calculated $\langle D \rangle_v$ data for the KY_3F_{10} nanoparticles is 36 ± 7 nm. Obtained nanoparticles have the same size, but the KY_3F_{10} phase shows wider size distribution.

It is worth to note that we obtained the cubic phase of the KYF_4 NPs only when the reaction mixture contains great excess (x10) of KF. In the case of stoichiometric mixture, obtained nanoparticles are cubic KY_3F_{10} phase. It allows suggesting that the limiting stage for the formation of crystalline phases in this system is diffusion of K^+ ions into the yttrium fluoride matrix.

The FT-IR absorption spectra (Figure 9) of the KYF_4 and KY_3F_{10} nanoparticles show the water content is present in both phases. They have broad absorption band around 3200 cm^{-1} , which corresponds to the stretching of the $-\text{OH}$ groups. The bands near 1300 and 1500 cm^{-1} correspond to the bending of the $-\text{OH}$ groups attached to the surface of nanoparticles and belonging to water molecules, respectively. The latter is only present in the KYF_4 phase. Most likely this intensive band is caused by the liquid water trapped in mesopores and this allows suggesting that only the KYF_4 nanoparticles contain significant amount of mesopores, while the KY_3F_{10} nanoparticles are almost free of mesopores. This result is in good

correlation with DT/TG analysis (see below). The bands around 700 cm^{-1} are related to yttrium fluoride bond [59]. The change of relative intensities and small shift are observed while comparing the KYF_4 and the KY_3F_{10} phases due to the different crystal structure of these compounds.

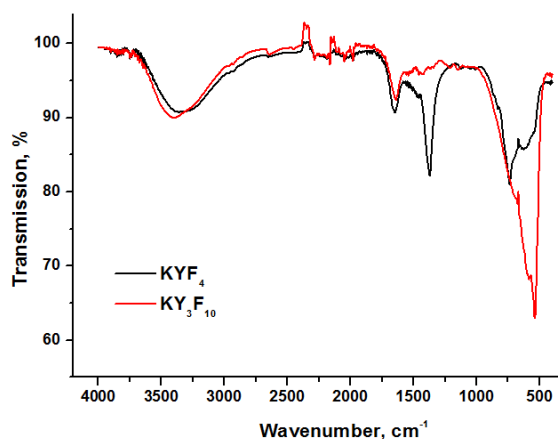


Figure 9. The FT-IR absorption spectra of the KYF_4 and the KY_3F_{10} nanoparticles.

4.2.2. Morphology and thermal behaviour of the synthesized nanoparticles

The morphology of synthesized nanoparticles obtained in different molar ratios, shows similar results. Figure 10 shows the TEM image of the KYF_4 nanoparticles. Obtained particles have isotropic shape and show rather uniform size distribution. The mean size of these nanoparticles is $31\pm 7\text{ nm}$, which is in good agreement with XRD results confirming the high crystallinity of obtained nanoparticles. The size distribution is close to normal. NPs contain some amount of mesopores. The formation of mesopores is related to the aggregation of primary nuclei in the formation process. Although nanoparticles are synthesized using biocompatible surfactant, they still show to be aggregated.

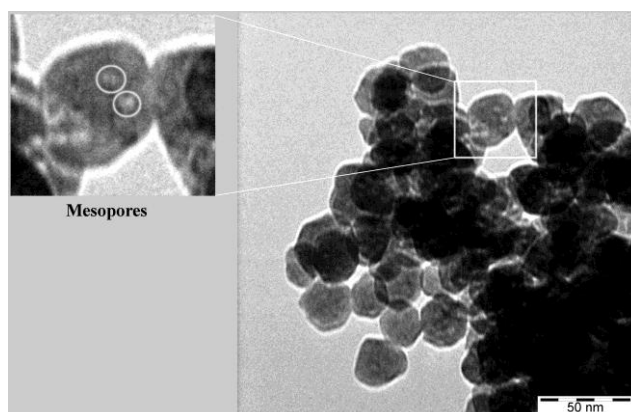


Figure 10. TEM image of the KYF_4 nanoparticles; the inset shows a zoomed fragment demonstrating the presence of the mesopores.

At the same time, the KY_3F_{10} nanoparticles synthesized in stoichiometric ratio show also isotropic shape, but wider size distribution (Figure 11). The mean size of obtained nanoparticles is 38 ± 13 nm and the size distribution of obtained nanoparticles is lognormal. Lognormal size distribution indicates that Oswald's ripening and recrystallization of nanoparticles occurs. The XRD data is also in a good correlation with TEM data, which indicates the good crystallinity of synthesized nanoparticles. The amount of mesopores in the volume of nanoparticles is much smaller compared to previously studied YPO_4 nanoparticles, probably due to lower rate of nucleation and more pronounced input of growth during fluorides formation.

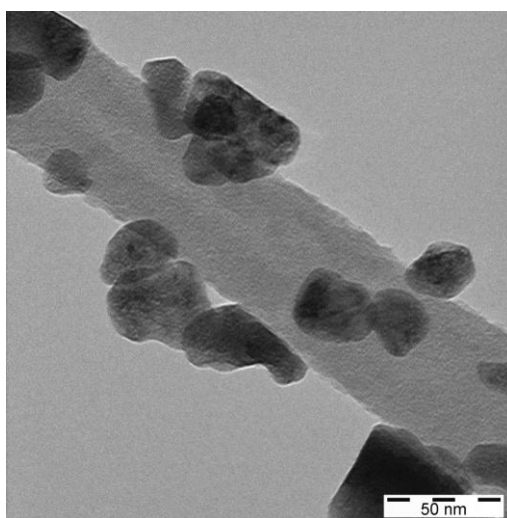


Figure 11. The TEM image of the KY_3F_{10} nanoparticles.

During the synthesis of the KYF_4 and the KY_3F_{10} nanoparticles, biocompatible surfactant Proxanol-268 is added to the reaction mixture in two different steps: to the solution of rare-earth ions (Sample 1) and to the already precipitated gel (Sample 2). The morphology and size of obtained nanoparticles are not changing, but the dispersability of obtained nanoparticles is different. The DLS data of the KYF_4 and the KY_3F_{10} nanoparticles (Figure 12) revealed that dispersing the Sample 1 in water gives the hydrodynamic radius of approximately 20 nm and a narrow size distribution. The particle size estimated from the TEM micrographs show slightly smaller size, but taking into account the fact that DLS radius is usually slightly overestimated, we may conclude that both phases prepared with first method result in more or less single nanoparticles in a solution. However, particles obtained by the second synthesis route (Sample 2) show much worse results compared to the Sample 1. The mean size for the KYF_4 nanoparticles is around 230 nm and for the KY_3F_{10} nanoparticles is around 190 nm.

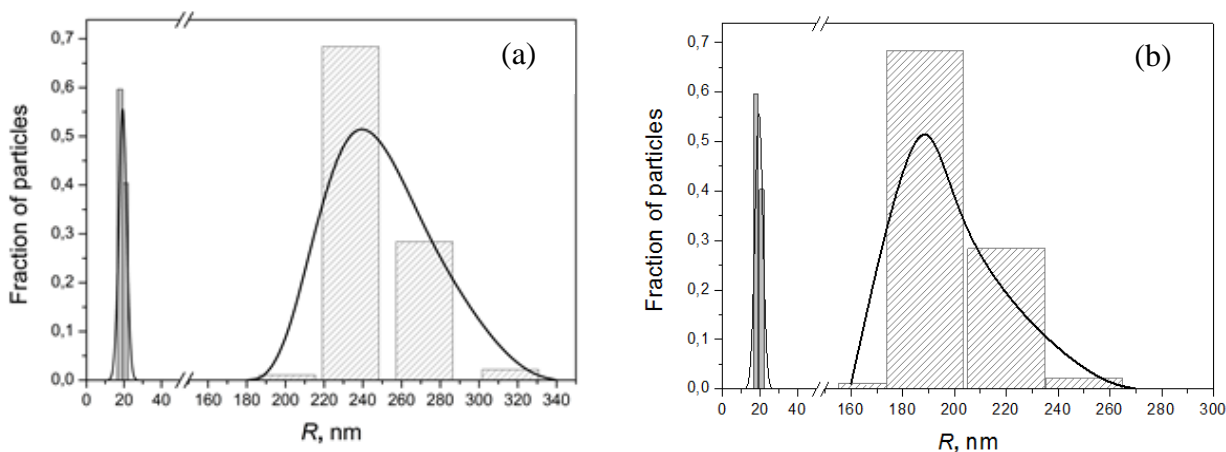


Figure 12. Hydrodynamic radii distribution for the KYF_4 particles (a) and the KY_3F_{10} particles (b) according to the DLS data: the Sample 1 (gray bars) and the Sample 2 (hatched bars).

The next task is to study the thermal behavior of the KYF_4 and the KY_3F_{10} phases. According to the data of TG/DTG-DTA analysis of the KYF_4 and the KY_3F_{10} phases (Figure 13), an overall weight loss in fluoride nanoparticles is remarkably smaller compared to the phosphate nanoparticles (Figure 6). The overall weight loss for the KYF_4 nanoparticles is 4.6%, which is almost twice smaller compared to the $\text{YPO}_4 \cdot 0.8\text{H}_2\text{O}$ nanoparticles. As it is seen from the DTG curve, there are two big minima, which correspond to the removal of physically adsorbed water molecules on the surface of nanoparticles and opening of mesopores. The first minimum observed around 105 °C is related to the removal of physically adsorbed H_2O molecules from the outer surface of nanoparticles. The temperature has shifted compared to previously described phosphate phases. This is probably due to the stronger binding of water molecules to fluoride surface. The weight loss at this temperature is significant (around 1%). This means, the outer surface of nanoparticles contain remarkable amount of physically adsorbed water. It is important to note that the data obtained from the differential thermal analysis (DTA) do not coincided to the DTG data. The first minimum of the DTA peak is around 128 °C, which is considerably higher than obtained from the DTG data. The shift is probably due to the distribution of the binding energies from physically sorbed water molecules (van der Waals interaction) to chemically sorbed water molecules (compensation unsaturated coordination of surface rare-earth ions). The second peak, according to the DTG data, occurs around 226 °C, which attributes to the opening of mesopores. The weight loss at this temperature is more than 3%. Again, the DTA data give dissimilar results with the DTG data. The second peak in the DTA curve occurs at 239°C, which is higher than the DTG peak. This is due to the fact that mesopores are located in different depths from the outer surface and open at different temperatures. The main weight loss occurs between 40 and 400

degrees, up to 4.3 %, which attributes mostly to removal of physically and chemically adsorbed water, opening of the mesopores and removal of the –OH molecular groups from the surface and the mesopores. At higher temperatures, analysis of exhaust gases does not show any traces of water vapours, so it is reasonable to suggest that further changes are due to phase transformations and/or oxidation of the fluoride nanoparticles. All the phases are very unstable and for that reason, the study on annealed samples cannot be conducted.

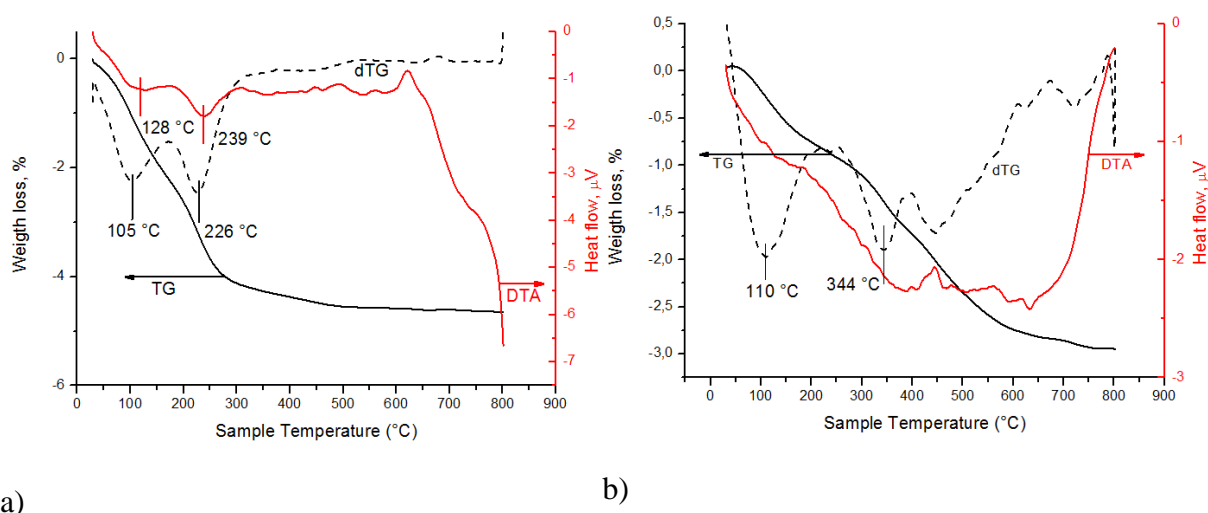


Figure 13. The TG/DTG-DTA data for the KYF_4 (a) and KY_3F_{10} (b) samples. In current graphs, some results are multiplied in order to draw out the graph. In graph (a) the DTG results are multiplied 100 times and in graph (b) the DTG results are multiplied 50 times and the TG results are multiplied twice.

The DTG/DTA for the KY_3F_{10} nanoparticles show considerably smaller amount of absorbed water. The overall weight loss for the KY_3F_{10} nanoparticles is only around 1 %, which makes the analysis rather difficult. The DTA curve shows constant endothermic effect, but not well-defined peaks. During the analysis, constant endothermic effect refers to the evaporation of absorbed water, opening of mesopores and removal of the –OH groups. The first DTG peak occurs at 110 °C, which corresponds to removal of physically sorbed H_2O and –OH groups from the outer surface of obtained nanoparticles. This is slightly higher than previously studied KYF_4 nanoparticles. The second peak at the DTG curve occurs at 344 °C, which correspond to the removal of strongly bound –OH groups and probably to the opening of mesopores. The weight loss in this case is around 0.5%, which indicates that amount of mesopores in this phase is very low. The reason of the lower content of mesopores in the KY_3F_{10} phase probably lies in the formation mechanism in which growth from feeding solution overwhelms nucleation. As well as the KYF_4 phase, above 400-450 °C there are no

traces of water vapours in the exhausted gases and changes are most likely due to phase transformations and oxidation.

Obtained results clearly show that the conditions of synthesis strongly affect phase composition (including water/-OH groups content), crystallinity and morphology of obtained nanoparticles. All these parameters strongly affect their luminescent properties. Study of this influence is the subject of the next chapter of the thesis.

4.3 Spectroscopic studies of synthesized nanoparticles

Luminescent properties of synthesized nanoparticles are also studied. The nanoparticles used in the study are: as-prepared and annealed samples of $\text{YPO}_4:\text{Nd}^{3+}$ phase; as-prepared samples of $\text{KYF}_4:\text{Nd}^{3+}$ and $\text{KY}_3\text{F}_{10}:\text{Nd}^{3+}$ phases. For fluorescence emission spectra measurements, $\text{YPO}_4:\text{Nd}^{3+}$ nanoparticles with higher dopant concentration (1%) are used. Meanwhile, for the fluorescence kinetics measurements of the $\text{YPO}_4:\text{Nd}^{3+}$ nanoparticles and other matrices, the samples are doped with low concentration of Nd^{3+} ion (0.1%).

The fluorescence emission spectrum of the 1 at% $\text{YPO}_4:\text{Nd}^{3+}$ nanoparticles at room temperature at 580 nm excitation wavelength. The fluorescence emission spectra of the $\text{KYF}_4:\text{Nd}^{3+}$ and the $\text{KY}_3\text{F}_{10}:\text{Nd}^{3+}$ nanoparticles are measured at room temperature and at 10 K with 576 nm excitation wavelength. After the excitation to the $^4\text{G}_{5/2}$ level of Nd^{3+} ion, the subsequent fast multiphonon relaxation to the $^4\text{F}_{3/2}$ metastable level occurs. (Figure 14)

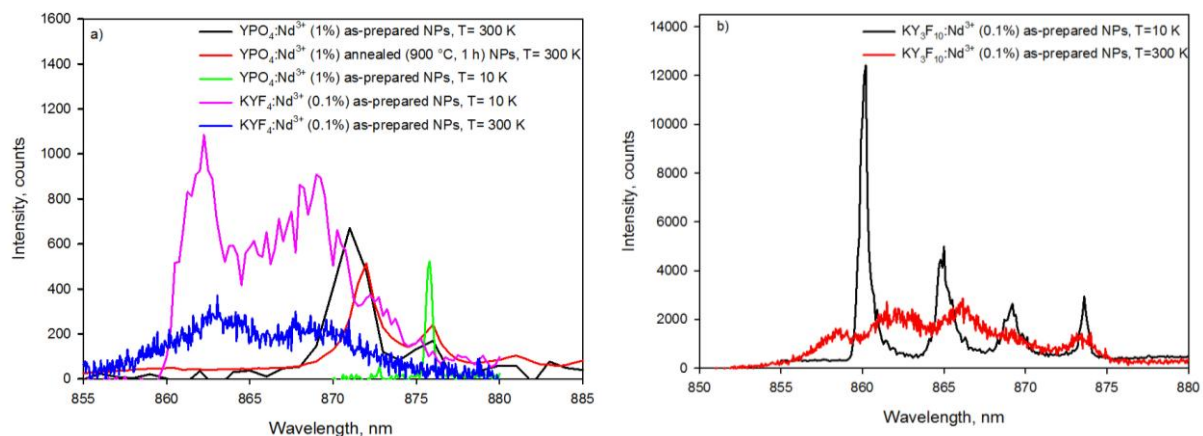


Figure 14. The fluorescence emission spectrum of the $\text{YPO}_4:\text{Nd}^{3+}$ NPs and the $\text{KYF}_4:\text{Nd}^{3+}$ NPs (a) and the $\text{KY}_3\text{F}_{10}:\text{Nd}^{3+}$ NPs (b).

Nd^{3+} ion have also two other fluorescence transitions, which are suitable for the imaging of biological tissue. These lines lie in 1 μm ($^4\text{F}_{3/2} \rightarrow ^4\text{I}_{11/2}$) and 1.3 μm ($^4\text{F}_{3/2} \rightarrow ^4\text{I}_{13/2}$) spectral bands, but they are not preferred, because the biological tissues are the most transparent in the 800-900 nm spectral band.

The fluorescence kinetics is measured for the as-prepared $\text{YPO}_4:\text{Nd}^{3+}$ nanoparticles, annealed $\text{YPO}_4:\text{Nd}^{3+}$ nanoparticles (annealed at 900 °C for 1 hour), as-prepared $\text{KYF}_4:\text{Nd}^{3+}$ nanoparticles (synthesized in water and D_2O) and as-prepared $\text{KY}_3\text{F}_{10}:\text{Nd}^{3+}$ nanoparticles. The fluorescence decay curves of the as-prepared samples, which are measured at the ${}^4\text{F}_{3/2} \rightarrow {}^4\text{I}_{9/2}$ transition of Nd^{3+} ion, display the non-exponential decay over the whole time range. The quenching process in Nd^{3+} doped nanoparticles can be related to two processes: energy transfer from the emitting ${}^4\text{F}_{3/2}$ level of Nd^{3+} ion to the vibrational levels of $-\text{OH}$ groups and Nd-Nd self-quenching [6, 7]. These processes can be accelerated by energy migration over Nd^{3+} ions (Figure 15).

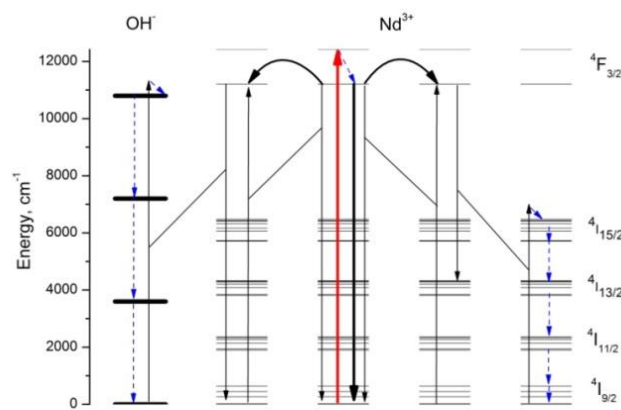


Figure 15. The scheme of relaxation of the ${}^4\text{F}_{3/2}$ metastable level of the Nd^{3+} ion in the doped crystalline nanoparticles. Red arrow – laser excitation, thick black arrow – near IR luminescence in the biological tissue transparency window, arc arrows – energy migration over Nd^{3+} ions to unexcited Nd^{3+} ions and to $-\text{OH}$ acceptors, thin black arrows - cross-relaxational transitions which govern nonradiative energy transfer, dashed arrows – multiphonon relaxation. Quenching channels: right –quenching caused by $-\text{OH}$ vibrations; left – self-quenching by unexcited Nd^{3+} ion.

The analysis of a probability of the excitation not to be quenched by the energy transfer processes to different acceptors (kinetics of impurity quenching $N(t)$) helps to estimate the mechanisms of fluorescence quenching and calculate parameters of energy migration. The kinetics of the impurity quenching $N(t)$ of the as-prepared samples can be obtained by division of the measured fluorescence kinetics $I_{\text{meas.}}(t)$ (normalized to unity) by $\exp\left(-\frac{t}{\tau_R}\right)$ in accordance with the following equation:

$$I_{\text{meas.}}(t) = N(t)\exp\left(-\frac{t}{\tau_R}\right) \quad (2)$$

Finding the correct radiative lifetime τ_R is important. Calculations from the as-prepared nanoparticles are very difficult, because of intensive quenching even at low concentrations. For the $\text{YPO}_4:\text{Nd}^{3+}$ nanoparticles, the fluorescence kinetics of as-prepared nanoparticles does not reach the spontaneous emission exponential stage within the measured time interval and the radiative lifetime cannot be determined even from the late stage of the kinetics. The radiative lifetime ($\tau_R=316 \mu\text{s}$) is obtained from annealed nanoparticles (900 °C, 1 hour), because annealing removes the $-\text{OH}$ groups and minimizes the fluorescence quenching (Figure 16).

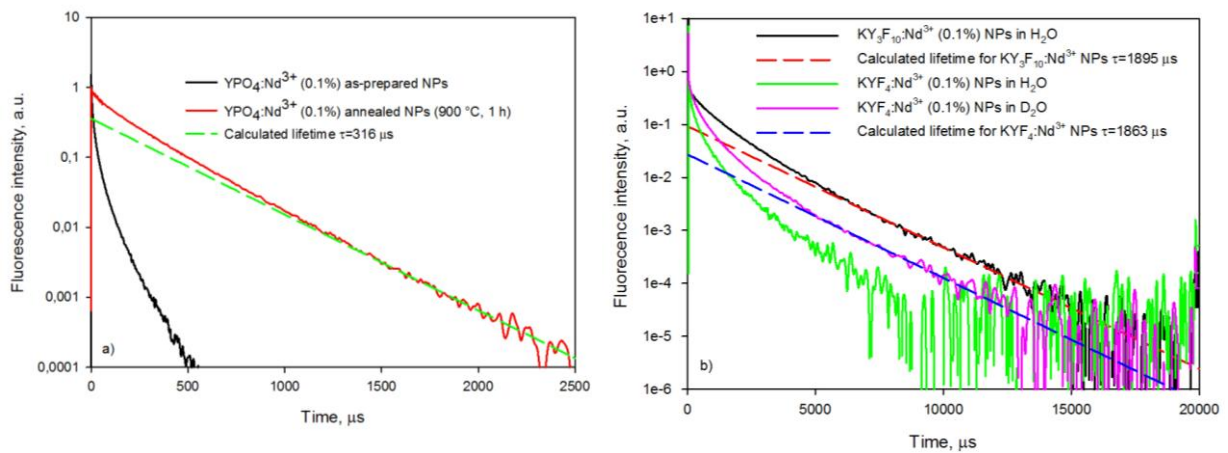


Figure 16. (a) Fluorescence kinetics of the $\text{YPO}_4:\text{Nd}^{3+}$ 0.1 at% NPs: as-prepared (black line) and annealed samples (red line). (b) Fluorescence kinetics of the $\text{KYF}_4:\text{Nd}^{3+}$ and the $\text{KY}_3\text{F}_{10}:\text{Nd}^{3+}$ NPs: the $\text{KY}_3\text{F}_{10}:\text{Nd}^{3+}$ NPs synthesized in water (black line), the $\text{KYF}_4:\text{Nd}^{3+}$ synthesized in H_2O (green line) and $\text{KYF}_4:\text{Nd}^{3+}$ synthesized in D_2O (pink line). The dashed lines are fitting by the exponential function.

For the fluoride nanoparticles, it is well seen the non-exponentiality of all kinetic curves (Figure 16b). The radiative lifetime ($\tau_R=1862 \mu\text{s}$) for the $\text{KYF}_4:\text{Nd}^{3+}$ nanoparticles is calculated from the kinetic curve obtained from the sample synthesized in D_2O , because the late stage of kinetic curve is exponential. The radiative lifetime ($\tau_R=1895 \mu\text{s}$) for the $\text{KY}_3\text{F}_{10}:\text{Nd}^{3+}$ nanoparticles is calculated from the nanoparticles synthesized in water. At this low concentration the relaxation of the excited electronic level at the latest stage of the kinetics is solely defined by the spontaneous emission. The radiative lifetimes for fluoride phases are nearly six times higher compared to the $\text{YPO}_4:\text{Nd}^{3+}$ nanoparticles. Both fluoride phases show relatively long radiative lifetime, which is enough to insure that that no biological tissue auto-fluorescence interfere the tumor imaging, since the autofluorescence is usually in nanoseconds

In very low Nd^{3+} concentrations (>0.1 at%), the Nd-Nd energy migration and self-quenching are negligible [8]. In this case the impurity quenching kinetics $N(t)$ is the static quenching or

direct energy transfer (DET) (excitation is dying in the place of origin). The excited Nd^{3+} ions act as energy donors and the $-\text{OH}$ acceptors act as the only fluorescence quenchers. The kinetics starts with the exponential ordered stage [7], continuing with the transitional region and the disordered Förster stage [60]. At the ordered stage, the energy is transferred to acceptors, which are located in the nearest coordination sphere. The acceptors located further from the donor ($R_{\text{DA}} \gg R_{\text{min}}$), are contributing mostly into the disordered Förster stage. The impurity quenching kinetics ($N_{\text{ord}}(t)$) at the initial exponential ordered stage is expressed as

$$N_{\text{ord}}(t) = \exp(-W_0 t) \quad (3)$$

valid at $t \rightarrow 0$, where the rate W_0 is defined as

$$W_0 = c_A C_{\text{DA}} \sum_{i=1}^N R_i^{-s} \quad (4)$$

where c_A is the relative acceptor concentration, C_{DA} is a microparameter of donor-acceptor interaction defined as $W_{\text{DA}} = C_{\text{DA}}/r^s$, a $\sum_{i=1}^N R_i^{-s}$ is the lattice sum over all acceptors sites, and s is the multipolarity of donor-acceptor interaction. The donor-acceptor interaction may be different types. In the case of energy transfer from the excited ${}^4\text{F}_{3/2}$ level of Nd^{3+} ion to vibrational levels of the $-\text{OH}$ molecular groups, the donor-acceptor interaction is dipole-dipole, so the $s=6$. [7]

If studying continuous medium with low donor and acceptor concentration ($R_{\text{DA}} \gg R_{\text{min}}$) and with arbitrary acceptor space dimension d , the disordered stage of static quenching kinetics is defined as

$$N(t) = \exp(-\gamma_A t^{\frac{d}{s}}) \quad (5)$$

To define the dimension of the acceptors space and estimate the location of acceptors, the kinetic curve is usually presented in the scales of $-\lg(-\ln[N(t)]) = \lg \gamma_A + (d/s) \lg t$. The slope of the curve determines the dimension of acceptor space d if the multipolarity s is known. The disordered static stage of the impurity quenching kinetics is linearized with a slope angle $\text{tg } \varphi = 1/2 = 3/6$, which results in $d=3$. It states that the acceptor space is three-dimensional and the acceptors are not located on the surface of nanoparticles, but in their volume [61].

For the $\text{YPO}_4:\text{Nd}^{3+}$ nanoparticles, one may observe the ordered stage, whereas for fluoride nanoparticles it is not seen. The TEM images revealed remarkable amount of mesopores located in the $\text{YPO}_4:\text{Nd}^{3+}$ nanoparticles. The first suggestion is that the $-\text{OH}$ acceptors are located in formed mesopores (Figure 4), which are filled with the mother solution. These

results are in good correlation with TGA results (Figure 6). However, this cannot be the only reason, because in this case, the donor-acceptor distance would be too large and the initial ordered stage that is detected could not have been observed. For that reason, it is important to find some other reason, why acceptors are located so close to the nearest coordination sphere of Nd^{3+} ion. It is probable that the crystal structure of synthesized nanoparticles have some defects, which allows $-\text{OH}$ groups to be located close to the donors. Since obtained nanoparticles are synthesized in water conditions, the protonation of the phosphate groups is possible. In this case, the minimal distance between the Nd^{3+} and $-\text{OH}$ groups is very short ($R_{\min} = 0.23 \text{ nm}$ [7]) and may cause strong fluorescence quenching. Current process can be described as:



For this study, nanoparticles were synthesized without pH adjustment and the HPO_4^{2-} is the most regnant form in the solution. It is probable that some of the HPO_4^{2-} groups remained in the structure of yttrium phosphate even after crystallization process. For sure, described process must be accompanied by charge compensation. This could be due to vacancy formation in a cationic sublattice or (less probable) replacement of Y^{3+} with a K^+ ion.

The fluoride nanoparticles do not have the first ordered stage, which means the $-\text{OH}$ quenchers are located further from the donor and no previously suggested protonation takes place. The $\text{KYF}_4:\text{Nd}^{3+}$ nanoparticles have also distinguishable mesopores (Figure 10), which contain $-\text{OH}$ quenchers. The TEM micrographs of KY_3F_{10} NPs (Figure 11) do not show visible mesopores, but the TGA results (Figure 13) indicate mass loss, which can be related to removal of absorbed water and opening of mesopores. Since all nanoparticles have quenchers located in three-dimensional space, one may conclude that applying a cover does not eliminate fluorescence quenching, as it is often believed.

In the case of $d=3$ and $s=6$, the energy transfer macroparameter is defined as [60]:

$$\gamma_A = \left(\frac{4}{3}\right) \pi^2 (n_A \sqrt{C_{DA}}) \quad (7)$$

The macroparameter can be determined from the replotted graph (Figure 17), where the scales are $\ln N(t)$ vs. $t^{1/2}$. The static quenching macroparameter γ_A is calculated from the slope angle tangent of the linear part of the curve. Obtained macroparameter for the $\text{YPO}_4:\text{Nd}^{3+}$ nanoparticles is $\gamma_A = 0.48 \mu\text{s}^{-1/2}$, whereas the calculated value of $\gamma_A = 0.11 \mu\text{s}^{-1/2}$ for the

KYF₄:Nd³⁺ NPs and $\gamma_A = 0.03 \mu\text{s}^{-1/2}$ for the KY₃F₁₀:Nd³⁺ NPs. This indicates that quenching in phosphate nanoparticles is stronger than in fluoride NPs.

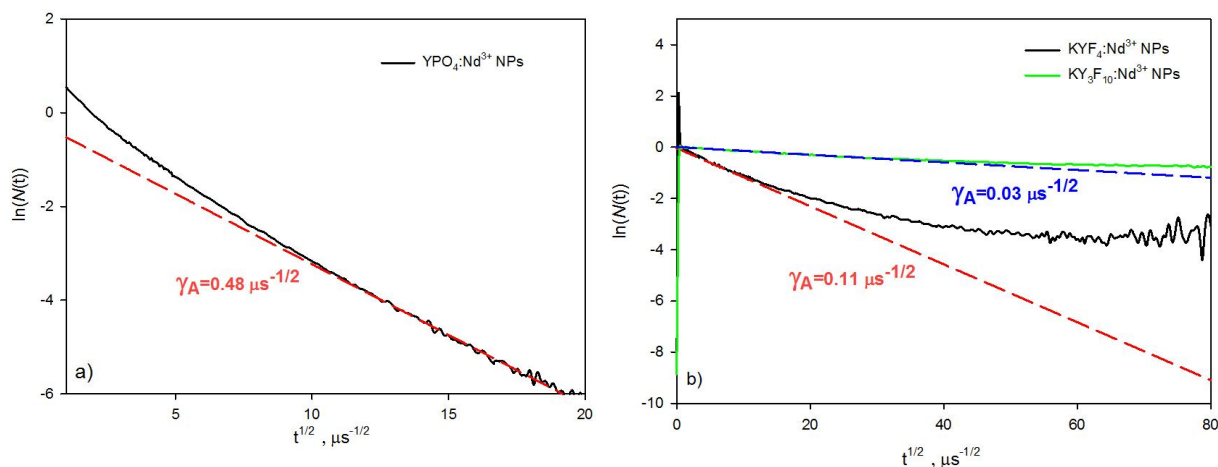


Figure 17. Impurity quenching kinetics $N(t)$ replotted as $\ln(N(t))$ vs. $t^{1/2}$. (a) the YPO₄:Nd³⁺ NPs (black line); (b) the KYF₄:Nd³⁺ (black line) and the KY₃F₁₀:Nd³⁺ NPs (green line). The dashed lines correspond to the fitting by the linear function.

To estimate the concentration of the –OH acceptors in the pores of the nanoparticles using Equation (7), assuming that C_{DA} (Nd-OH) = 0.6 nm⁶ ms⁻¹ [7] found for phosphate laser glass does not differ strongly from that of the Nd³⁺ doped phosphate crystalline nanoparticles. The calculated concentration of the –OH groups in the YPO₄:Nd³⁺ NPs is high ($n_A(\text{OH}) = 2.7 \text{ nm}^{-3}$) compared to the Nd³⁺ concentration ($n_A(\text{Nd}^{3+}) = 0.14 \text{ nm}^{-3}$). The minimum distance between Nd³⁺ ions ($R_{\min}(\text{Nd-Nd}) = 0.38 \text{ nm}$ [7]) is longer than the distance between Nd³⁺ ion and –OH groups ($R_{\min}(\text{Nd-OH}) \approx 0.23 \text{ nm}$ [7]). A very steep dependence of the probability of the energy transfer on the distance R between the Nd³⁺ donor and both types of acceptors

$$W_{DA} = C_{DA}/R^6 \quad (8)$$

explains a negligible role of Nd-Nd self-quenching.

The –OH acceptor concentration is estimated in the fluoride phases in comparison to the YPO₄:Nd³⁺ nanoparticles. Since the $C_{DA}^{\text{Nd-OH}}$ microparameter is proportional to the spontaneous emission rate $1/\tau_R$ of the donor [62], and the ratio of the $C_{DA}^{\text{Nd-OH}}$ microparameters can be therefore roughly estimated from the ratio of spontaneous emission rates in the two materials, considering that $C_{DA}^{\text{Nd-OH}} = 0.6 \text{ nm}^6/\text{ms}$ for the phosphate nanocrystals. The spontaneous emission rate $1/\tau_R$ is approximately 6 times higher in the phosphate nanoparticles than in fluoride ones. Assuming that the overlap integrals of the

form-factors of the Nd^{3+} fluorescence spectrum and the $-\text{OH}$ absorption spectrum in phosphates and fluorides are close, we may estimate $C_{DA}^{\text{Nd-OH}} \sim 0.1 \text{ nm}^6/\text{ms}$ for the fluoride nanoparticles. Using the Equation (7), we may therefore conclude that the concentration of the $-\text{OH}$ acceptors in the $\text{KYF}_4:\text{Nd}^{3+}$ nanoparticles is approximately 1.24 nm^{-3} , i.e. about twice lower than that in the phosphate nanoparticles (2.7 nm^{-3}). The concentration of the $-\text{OH}$ acceptors in the $\text{KY}_3\text{F}_{10}:\text{Nd}^{3+}$ nanoparticles is approximately 0.40 nm^{-3} , i.e. approximately seven times lower than that in the phosphate nanoparticles and more than three times lower than in the $\text{KYF}_4:\text{Nd}^{3+}$.

The water content in the $\text{KY}_3\text{F}_{10}:\text{Nd}^{3+}$ NPs is remarkably lower compared to the $\text{KYF}_4:\text{Nd}^{3+}$ and the $\text{YPO}_4:\text{Nd}^{3+}$ NPs. The spectroscopy results are in good correlation with the TG data, where the overall water content was also remarkably lower compared to other nanoparticles. Also, the TEM images confirmed that the $\text{KY}_3\text{F}_{10}:\text{Nd}^{3+}$ nanoparticles are smaller compared to $\text{YPO}_4:\text{Nd}^{3+}$ NPs and the XRD results revealed higher crystallinity. This allows suggesting that mesopores in $\text{KY}_3\text{F}_{10}:\text{Nd}^{3+}$ nanoparticles are smaller compared to other phases.

As mentioned in ref. [3], it is possible to determine the luminescence quantum yield using different approaches. In this work, the relative fluorescence quantum yield is calculated as the ratio $\frac{\eta}{\eta_0}$ of quantum yield of luminescence because of impurity quenching η [63]:

$$\eta = \frac{1}{\tau_R} \int_0^{\infty} N(t) \exp\left(-\frac{t}{\tau_D}\right) dt \quad (9)$$

where τ_D is the lifetime in the absence of quenching energy transfer, to the quantum yield η_0 in the absence of quenching energy transfer.

$$\eta_0 = \frac{1}{\tau_R} \int_0^{\infty} \exp\left(-\frac{t}{\tau_D}\right) dt = \frac{\tau_D}{\tau_R} = \frac{\tau_N}{\tau_N + \tau_R} \quad (10)$$

where τ_N is the lifetime of the intracenter quenching. The relative luminescence quantum yield for the metastable $^4\text{F}_{3/2}$ level of Nd^{3+} ion, with $\eta_0=1$ is expressed as

$$\eta = \frac{\int_0^{\infty} N(t) \exp\left(-\frac{t}{\tau_R}\right) dt}{\tau_R} = \frac{\int_0^{\infty} I_{meas.}(t) dt}{\tau_R} \quad (11)$$

and is equal to the absolute quantum yield of luminescence from the $^4\text{F}_{3/2}$ metastable level.

The Table 2 shows calculated fluorescence quantum yield values using Equation (11) for all the studied matrices, together with the other characteristic values.

Table 2. The negative correlation between the fluorescence quantum yields η of the ${}^4F_{3/2}$ level of Nd^{3+} and the Förster macroparameters of energy transfer γ_A (Nd-OH) in different 0.1% Nd^{3+} doped nanocrystals.

Type of nanocrystal matrix	TEM sizes, nm	τ_R , μs	γ_A , $\mu\text{s}^{-1/2}$	η , %
YPO_4	41±12	316	0.48	4.8
cubic KYF_4	31±7	1862	0.11	9.8
KY_3F_{10}	38±13	1895	0.03	38.2

The highest value of the fluorescence quantum yield is calculated for the $\text{KY}_3\text{F}_{10}:\text{Nd}^{3+}$ nanoparticles. This is approximately 4 times higher compared to the $\text{KYF}_4:\text{Nd}^{3+}$ nanoparticles and 8 times higher compared to the phosphate nanoparticles. It should be also noted that it is in negative correlation with the Förster macroparameter of quenching energy transfer (γ_A), i.e. the lower the quenching by the volumetric –OH acceptors, the higher is the fluorescence quantum yield. The fluorescence is less quenched in the $\text{KY}_3\text{F}_{10}:\text{Nd}^{3+}$ nanoparticles and therefore the fluorescence quantum yield is the highest, which makes them especially promising materials for bioimaging.

Acknowledgements

The author would like to thank her supervisors Dr. A. S. Vanetsev and Dr. hab. Yu. V. Orlovskiy for the help and guidance during the preparation of the current work. Also the other group members M.Sc. E.V. Samsonova, K. Kaldvee, L. Puust and Dr. A.V. Popov for the spectroscopic measurements, Dr. U. Mäeorg and Dr. U. Joost for the FT-IR measurements. Author would like to thank the Laboratory of Laser Spectroscopy in Institute of Physics for the help and support during the preparation of current work.

5. Conclusions

A synthetic procedure is developed, which allows controlling phase composition, morphology, and dispersibility of yttrium phosphates and fluorides doped with Nd^{3+} ions. Suggested procedure is based on the microwave-hydrothermal treatment of freshly precipitated gels in well-defined conditions, including temperature, duration of treatment, reagents concentration, surfactant concentration, and pH of media.

Conditions of formation of the $\text{YPO}_4 \cdot 0.8\text{H}_2\text{O}$ phase in hydrothermal conditions are established. It is shown that large excess of either PO_4^{3-} or OH^- ions in the reaction mixture is necessary for the synthesis of the hexagonal hydrate of yttrium orthophosphate. The mechanism of the $\text{YPO}_4 \cdot 0.8\text{H}_2\text{O}$ phase stabilization at elevated temperatures is clarified. It was shown that despite the almost complete removal of crystalline water below $300\text{ }^\circ\text{C}$, some amount of strongly bound $-\text{OH}$ groups remain in the structure up to $550\text{ }^\circ\text{C}$ and stabilizes the hexagonal structure.

Highly crystalline and water dispersible nanoparticles of Nd^{3+} -doped KYF_4 and KY_3F_{10} were synthesized. It was shown that large excess of F^- ions is needed to obtain nanoparticles of metastable cubic KYF_4 phase, which does not exist in bulk state. By the means of thermal analysis and IR spectroscopy, it was established that the KYF_4 phase contains substantial amount of mesopores, while the KY_3F_{10} nanoparticles are almost free of them. Conditions for preparation of high quality water colloids of synthesized nanoparticles were established

The luminescent properties of synthesized Nd^{3+} -doped yttrium phosphates and fluorides nanoparticles were studied. Structural origins of fluorescence quenching are revealed. It was shown that protonation of the PO_4^{3-} group in phosphate nanoparticles leads to intensive quenching, resulting in two-stage kinetics, which is caused by the vibrations of the $-\text{OH}$ groups located in the volume of NPs. Meanwhile, the fluorescence from the fluoride nanoparticles is also quenched by the $-\text{OH}$ vibrations, but it is remarkably less compared to the phosphate nanoparticles due to the absence of protonation and smaller amount of mesopores in the volume of the NPs, especially in the $\text{KY}_3\text{F}_{10}:\text{Nd}^{3+}$ nanoparticles. This increases several times the fluorescence quantum yield for the latter and makes it especially promising material for bioimaging in the first transparency window of biological tissues.

The results discussed in this work are published:

1. Vanetsev, A.S., Samsonova, E.V., Gaitko, O.M., Keevend, K., Popov, A.V., Mäeorg, U., Mändar, H., Sildos, I., Orlovskii, Yu.V. Phase composition and morphology of nanoparticles of yttrium orthophosphates synthesized by microwave-hydrothermal treatment: the influence of synthetic conditions. *Journal of Alloys and Compounds*. 2015, 639, 415-421.
2. Samsonova, E.V., Popov, A.V., Vanetsev, A.S., Keevend, K., Orlovskaya, E.O., Kiisk, V., Lange, S., Joost, U., Kaldvee, K., Mäeorg, U., Glushov, A.N., Ryabova, A.V., Sildos, I., Osiko, V.V., Steiner, R., Losvhenov, V.B., Orlovskii, Yu.V. An energy transfer probe for –OH-quenchers in the Nd³⁺:YPO₄ nanocrystals suitable for imaging in the biomedical tissue transparency window. *Phys. Chem. Chem. Phys.* 2014, 16, 26806.
3. Samsonova, E.V., Popov, A.V., Vanetsev, A.S., Keevend, K., Kaldvee, K., Puust, L., Baranchikov, A.E., Ryabova, A.V., Fedorenko, S.G., Kiisk, V., Sildos, I., Kikas, J., Steiner, R., Losvhenov, V.B., Orlovskii, Yu.V. Fluorescence quenching mechanism for water-dispersible Nd³⁺:KYF₄ nanoparticles synthesized by microwave-hydrothermal technique. *J. Lumin.* 2015, <http://dx.doi.org/10.1016/j.jlumin.2015.03.015>

6. Mikrolaine hüdrotërmaalse meetodiga sünteesitud vees disperseeritavad luminesseeruvad neodüümiga dopeeritud ütrium fosfaadi ja fluoriidi nanoosakesed.

Kerda Keevend

Kokkuvõte

Kuigi meditsiin on viimase 30 aastaga palju arenenud, on vähki suuremus jätkuvalt väga kõrge. Nõrgestatud organisme peab uurima väheinvasiivsete meetoditega. Selleks sobib laserindutseeritud ravi, kus kasutatakse lähinfrapunases spektrivahemikus kiirgavaid nanoosakesi. Selles piirkonnas asub eluskoe läbilaskvuspiirkond, kus rakkude neeldumine on väike. Antud töö eesmärgiks oli välja töötada sünteesiprotokoll vees disperseeritavate luminesseerivate ütrium fosfaadi ja fluoriid nanoosakesete jaoks, kasutades mikrolaine hüdrotërmaalset meetodit, uurida nende luminesentsi omadusi ning hinnata materjali sobivust biomeditsiini rakenduseks.

Töös kasutatavad nanoosakesed sünteesiti mikrolaine hüdrotërmaalse meetodiga. Ühendeid karakteriseeriti mitmete meetoditega: röntgendifraktsioon analüüs, infrapunaspetskoopia, läbivalgustav elektronmikroskoopia, termogravimeetria ja fluoretsentsspetskoopia.

Kokkuvõttes töötati välja sünteesiprotokoll mikrolaine hüdrotërmaalse meetodi jaoks, mis aitab kontrollida Nd^{3+} iooniga dopeeritud ütrium fosfaatide ja fluoriidide faasilist koostist, morfoloogiat ning disperseeritavust vees. Välja pakutud protokoll hõlmab kontrolli mitmete reaktsioonitingimuste üle.

Leiti tingimused $\text{YPO}_4 \cdot 0.8\text{H}_2\text{O}$ nanoosakeste sünteesiks. Reaktsioonisegusse suures ülehulgas lisatud PO_4^{3-} või OH^- ioonid on vajalikud mainitud faasi sünteesimiseks. Töös näidatakse, et kuumutamisel eraldub suurem osa kristallveest allpool $300\text{ }^\circ\text{C}$, kuid osa vee molekulide jääb struktuuri stabiliseerima kuni $550\text{ }^\circ\text{C}$ -ni. Lisaks töötati välja sobivad tingimused kristalliliste ning vees disperseeritavate Nd^{3+} iooniga dopeeritud KYF_4 ja KY_3F_{10} nanoosakeste sünteesiks. Näidati, et reaktsioonisegusse suures ülehulgas olevad F^- ioonid aitavad kaasa metastabiilsete KYF_4 nanoosakeste moodustamiseks, mida on kirjeldatud vaid nano-olekus. Infrapunaspetskoopia ning termogravimeetria tulemused tõestasid, et antud faas sisaldab suures hulgas vett, samal ajal kui KY_3F_{10} faas on praktiliselt veevaba.

Sünteesitud nanoosakeste luminesentsomadusi uuriti fluorestsents-spektroskoopia ning fluorestsentsi kineetika meetodite abil. Nanoosakeste struktuurilistele eripäradele tuginedes leiti fluorestsentsi kustutamise mehhanism. Pakuti välja fosfaatrühma protoneerimise mudel, mis kirjeldab väga hästi kaheastmelist fluorestsentsi kustutamise kineetikat, mis on põhjustatud hüdroksüülrühmade vibratsioonvõnkumistest. Samal ajal sünteesitud fluoriidi nanoosakeste fluorestsents on samuti kustutatud –OH rühmade poolt, kuid võrreldes fosfaatidega oluliselt vähemal määral, kuna eespool kirjeldatud protoneerimist ei toimu ning osakesed sisaldavad vähemal määral mesopore. Seetõttu on fluorestsentsi kvantsaagis mitmeid kordi kõrgem KY_3F_{10} nanoosakestes võrreldes teistega osakestega, mis muudab nad paljulubavateks fluorestsentsmarkeriteks.

7. References

- [1] Jemal, A., Siegel, R., Xu, J., Ward, E., “Cancer Statistics, 2010,” *Ca-Cancer J- Clin*, vol. 60, 2010.
- [2] Bünzli, J.-C. G., “Lanthanide Luminescence for Biomedical Analyses and Imaging,” *Chem. Rev.*, no. 110, pp. 2729-2755., 2010.
- [3] Gai, S., Li, C., Yang, P., Lin, J., “Recent Progress in Rare Earth Micro/Nanocrystals: Soft Chemical Synthesis, Luminescent Properties, and Biomedical Applications.,” *Chem. Rev.*, vol. 114, pp. 2343-2389, 2014.
- [4] Ryabova, A.V., Pominova, D. V., Krut'ko, V.A., Komora, M. G., Lochenov, V.B., “Spectroscopic research of upconversion nanomaterials based on complex oxide compounds doped with rare-earth ion pairs: benefit for cancer diagnostics by upconversion fluorescence and radio sensitive methods,” *Photonics Lasers Med.*, no. 2, p. 117, 2013.
- [5] Glushkov, N.A., Basiev, T.T., Orlovskii, Yu. V., “Kinetics of the direct energy transfer of optical excitation in crystalline nanoparticles: Theory and Monte Carlo computer simulation.,” *Nanotechnol. Russ.*, no. 4, p. 722, 2009.
- [6] Samsonova, E.V., Popov, A.V., Vanetsev, A.S., Keevend, K., Kaldvee, K., Puust, L., Baranchikov, A.E., Ryabova, A.V., Fedorenko, S.G., Kiisk, V., Sildos, Kikas, J., Steiner, R., Loschenov, V.B. Orlovskii, Yu. V., “Fluorescence quenching mechanism for water-dispersible $\text{Nd}^{3+}:\text{KYF}_4$ nanoparticles synthesized by microwave-hydrothermal technique.,” *Journal of Luminescence*, 2015.
- [7] Samsonova, E.V., Popov, A.V., Vanetsev, A.S., Keevend, K., Orlovskaya, E.O., Kiisk, V., Lange, S., Joost, U., Kaldvee, K., Mäeorg, U., Glushkov, N.A., Ryabova, A.V., Sildos, I., Osiko, V.V., Steiner, R., Loschenov, V.B. Orlovskii, Yu. V. , “An energy transfer kinetic probe for OH quenchers in the $\text{Nd}^{3+}:\text{YPO}_4$ nanocrystals suitable for imaging in the biological tissue transparency window,” *Phys. Chem. Chem. Phys.*, vol. 16, pp. 26806-26815, 2014.
- [8] Orlovskii, Yu. V., Popov, A.V., Platonov, V.V., Fedorenko, S.G., Sildos, I., Osipov, V.V., “Fluctuation kinetics of fluorescence hopping quenching in the $\text{Nd}^{3+}:\text{Y}_2\text{O}_3$ spherical nanoparticles,” *Journal of Luminescence*, vol. 139, p. 91–97, 2013.
- [9] Zhang, X.-D., Wu, H.-Y., Wu, D., Wang, Y.-Y., Chang, J.-H., Zhai, Z.-B., Meng, A.-M., Liu, P.-X., Zhang, L.-A., Fan, F.-Y., “Toxicologic effects of gold nanoparticles in vivo by different administration routes,” *International Journal of Nanomedicine*, vol. 5, pp. 771-781, 2010.
- [10] Buzea, C., Pacheco, I.I., Robbie, K., “Nanomaterials and nanoparticles: Sources and Toxicity,” *Biointerphases*, vol. 2, no. 4, p. MR17, 2007.
- [11] Zhou, S., Liu, X., Wang, D. , “Si/TiSi₂ Heteronanostructures as High-Capacity Anode Material for Li Ion Batteries,” *Nano Lett.*, vol. 10, no. 3, pp. 860-863, 2010.

- [12] Lee, S.S., Song, W., Cho, M., Puppala, H.L., Nguyen, P., Zhu, H., Segatori, L., Colvin, V.L., "Antioxidant Properties of Cerium Oxide Nanocrystals as a Function of Nanocrystal Diameter and Surface Coating," *ACS Nano*, vol. 7, no. 11, pp. 9693-9703, 2013.
- [13] Taylor, R.A., Otanicar, T., Rosengarten, G., "Nanofluid-based optical filter optimization for PV/T systems," *Light: Science & Applications*, vol. 1, 2012.
- [14] Buil, M.L., Esteruelas, M.A., Niembro, S., Oliván, M., Orzechowski, L., Pelayo, C., Vallribera, A., "Dehalogenation and Hydrogenation of Aromatic Compounds Catalyzed by Nanoparticles Generated from Rhodium Bis(imino)pyridine Complexes," *Organometallics*, vol. 29, no. 19, pp. 4375-4383, 2010.
- [15] Labhasetwar, V., Leslie-Pelecky, D.L. *Biomedical Applications of Nanotechnology*, New Jersey: Wiley&Sons, 2007.
- [16] Laurent, S., Forge, D., Porty, M., Roch, A., Robic, C., Vander Elst, L., Muller, R.N., "Magnetic Iron Oxide Nanoparticles: Synthesis, Stabilization, Vectorization, Physicochemical Characterization, and Biological Applications," *Chem. Rev.*, vol. 108, no. 6, pp. 2064-2110, 2008.
- [17] Jaque, D., Maestro, L.M., del Rosal, B., Haro-Gonzalez, P., Benayas, A., Plaza, J.L., Rodriguez, E.M., Sole, J.G., "Nanoparticles for photothermal therapies," *Nanoscale*, vol. 6, p. 9494, 2014.
- [18] Blanco-Andajuar, C., Tung, L.D., Thanh, N.T.K., "Synthesis of nanoparticles for biomedical applications," *Annu. Rep. Prog. Chem., Sect. A*, vol. 106, pp. 553-568, 2010.
- [19] Patra, C.R., Bhattacharya, R., Wang, E., Katarya, A., Lau, J.S., Dutta, S., Murders, M., Wang, S., Buchrow, S.A., Safgren, S.L., Yaszemski, M.J., Reid, J.M., Ames, M.M., Mukherjee, P., Mukhopadhyay, D., "Targeted Delivery of Gemcitabine to Pancreatic Adenocarcinoma Using Cetuximab as a Targeting Agent," *Cancer Res.*, vol. 68, no. 6, pp. 1970-1978, 2008.
- [20] Schneider, B.H., Dickinson, E.L., Vach, M.D., Hoijer, J.V., Howard, L.V., "Highly sensitive optical chip immunoassays in human serum," *Biosens. Bioelectron.*, vol. 15, pp. 13-22, 2000.
- [21] Santra, S., Tapeç, R., Theodoropoulou, N., Dobson, J., Hebard, A., Tan, W., "Synthesis and Characterization of Silica-Coated Iron Oxide Nanoparticles in Microemulsion: The Effect of Nonionic Surfactants," *Langmuir*, vol. 17, no. 10, pp. 2900-2906, 2001.
- [22] Shan, J., Ju, Y., "A single-step synthesis and the kinetic mechanism for monodisperse and hexagonal-phase NaYF₄:Yb,Er upconversion nanophosphors," *Nanotechnology*, vol. 20, p. 275603, 2009.
- [23] Zhou, J., Liu, Q., Feng, W., Sun, Y., Li, F., "Upconversion Luminescent Materials: Advances and Applications," *Chem. Rev.*, vol. 115, pp. 395-465, 2015.
- [24] Basiev, T.T., Dergachev, A.Yu., Orlovskii, Yu.V., Prokhorov, A.M., "Multiphonon nonradiative relaxation from high-lying levels of Nd³⁺ ions in fluoride and oxide laser materials," *J. Lumin.*, vol. 53, pp. 19-23, 1992.
- [25] Xu, W., Bai, X., Xu, S., Zhu, Y., Xia, L., Song, H., "Remarkable fluorescence

- enhancement in $\text{YVO}_4:\text{Eu}^{3+}@\text{Ag}$ nano-hybrids induced by interface effects.” *RSC Advances*, vol. 2, pp. 2047-2054, 2012.
- [26] Bear, J.C., Yu, B., Blanco-Andujar, C., McNaughter, P.D., Sounthern, P., Mafina, M.-K., Pankhurst, Q.A., Parkin, I.P., “A low cost synthesis method for functionalised ion oxide nanoparticles for magnetic hyperthermia from readily available materials,” *Faraday Discuss*, vol. 175, pp. 83-95, 2014.
- [27] Zhang, L., He, R., Gu, H., “Oleic acid coating on the monodisperse magnetite nanoparticles,” *Applied Surface Science*, vol. 253, no. 5, pp. 2611-2617, 2006.
- [28] Gainer, C.F., Romanowski, M., “A review of synthetic methods for the production of upconverting lanthanide nanoparticles,” *J. Innov. Opt. Health Sci.*, vol. 7, no. 2, p. 1330007 (11 pages), 2014.
- [29] Li, C., Lin, J., “Rare earth fluoride nano-/microcrystals: synthesis, surface modification and application,” *J. Mater. Chem.*, vol. 20, pp. 6831-6847, 2010.
- [30] Zou, P., Hong, X., Ding, Y., Zhang, Z., Chu, X., Shaymurat, T., Shao, C., Liu, Y., “Up-Conversion Luminescence of $\text{NaYF}_4:\text{Yb}^{3+}/\text{Er}^{3+}$ Nanoparticles Embedded into PVP Nanotubes with Controllable Diameters,” *J. Phys. Chem. C*, vol. 116, pp. 5787-5791, 2012.
- [31] Bogdan, N., Vetrone, F., Ozin, G.A., Capobianco, J.A., “Synthesis of Ligand-Free Colloidally Stable Water Dispersible Brightly Luminescent Lanthanide-Doped Upconverting Nanoparticles,” *Nano Lett.*, vol. 11, pp. 835-840, 2011.
- [32] Massart, R., “Preparation of Aqueous Magnetic Liquids in Alkaline and Acidic Media,” *IEEE Transactions on Magnetics*, Vols. MAG-17, no. 2, 1981.
- [33] Babes, L., Denizot, B., Tanguy, G., Le Jeune, J. J., Jallet, P., “Synthesis of Iron Oxide Nanoparticles Used as MRI Contrast Agents: A Parametric Study,” *J. Colloid Interface Sci.*, vol. 212, no. 2, pp. 474-482, 1999.
- [34] Aubry, P., Bensalah, A., Gredin, P., Patriarche, G., Vivien, D., Mortier, M., “Synthesis and optical characterization of Yb-doped CaF_2 ceramics,” *Optical Materials*, vol. 31, pp. 750-753, 2009.
- [35] Mai, M., Feldmann, C., “Microemulsion-based synthesis and luminescence of nanoparticulate CaWO_4 , ZnWO_4 , $\text{CaWO}_4:\text{Tb}$, and $\text{CaWO}_4:\text{Eu}$,” *J. Mater. Sci.*, vol. 47, pp. 1427-1435, 2012.
- [36] [Online]. Available: http://shodhganga.inflibnet.ac.in/bitstream/10603/11272/11/11_chapter%203.pdf. [Accessed 22. May 2015].
- [37] Vaidya, S., Rastogi, P., Agarwal, S., Gupta, S.K., Ahmad, T., Antonelli, A.M.Jr., Ramanujachary, K.V., Lofland, S.E., Ganguli, A.K., “Nanospheres, Nanocubes, and Nanorods of Nickel Oxalate: Control of Shape and Size by Surfactant and Solvent,” *J. Phys. Chem. C*, vol. 112, pp. 12610-12615, 2008.
- [38] Byrappa, K., Yoshimura, M., *The handbook of hydrothermal technology. A technology for Crystal Growth and Materials Processing.*, New Jersey: Noyes Publications, 2001.

- [39] Demazeau, G., Largeteau, A., "Hydrothermal/Solvothermal Crystal Growth: an Old but Adaptable Process," *Z. Anorg. Allg. Chem.*, vol. 641, no. 2, pp. 159-163, 2015.
- [40] Li, H., Lu, Z., Cheng, G., Rong, K., Chen, F., Chen, R., "HEPES-involved hydrothermal synthesis of Fe₃O₄ nanoparticles and their biological application," *RSC Adv.*, vol. 5, pp. 5059-5067, 2015.
- [41] Lawrence, G., Baskar, A.V., El-Newehy, M.H., Cha, W.S., Al-Deyab, S.S., Vinu, A., "Quick high-temperature hydrothermal synthesis of mesoporous materials with 3D cubic structure for the adsorption of lysozyme," *Sci. Technol. Adv. Mater.*, vol. 16, pp. 024806-024817, 2015.
- [42] Ortiz-Landeros, J., Gomez-Yanez, C., Lopez-Juarez, R., Davalos-Velasco, I., Pfeiffer, H., "Synthesis of advanced ceramics by hydrothermal crystallization and modified related methods," *Journal of Advance Ceramics*, vol. 1, no. 3, pp. 204-220, 2012.
- [43] Zhang, F., Zhao, D., "Synthesis of Uniform Rare Earth Fluoride (NaMF₄) Nanotubes by In Situ Ion Exchange from Their Hydroxide [M(OH)₃] Parents," *ACS Nano*, vol. 3, no. 1, pp. 159-164, 2009.
- [44] He, F., Yang, P., Wang, D., Niu, N., Gai, S., Li, X., "Self-Assembled β -NaGdF₄ Microcrystals: Hydrothermal Synthesis, Morphology Evolution, and Luminescent Properties," *Inorg. Chem.*, vol. 50, pp. 4116-4124, 2011.
- [45] Cao, T., Yang, Y., Gao, Y., Zhou, J., Li, Z., Li, F., "High-quality water-soluble and surface-functionalized upconversion nanocrystals as luminescent probes for bioimaging," *Biomaterials*, vol. 32, pp. 2959-2968, 2011.
- [46] Wang, X., Zhuang, J., Peng, Q., Li, Y., "A general strategy for nanocrystal synthesis," *Nature*, vol. 437, no. 7055, pp. 121-124, 2005.
- [47] Byrappa, K., Adschiri, T., "Hydrothermal technology for nanotechnology," *Progress in Crystal Growth and Characterization of Materials*, vol. 53, pp. 117-166, 2007.
- [48] Li, F., Li, C., Liu, X., Chen, Y., Bai, T., Wang, L., Shi, Z., Feng, S., "Hydrophilic, Upconverting, Multicolor, Lanthanide-Doped NaGdF₄ Nanocrystals as Potential Multifunctional Bioprobes," *Chem. Eur. J.*, vol. 18, pp. 11641-11646, 2012.
- [49] Stadler, A., Yousefi, B.H., Dallinger, D., Walla, P., Van der Eycken, E., Kaval, N., Kappe, C.O., "Scalability of Microwave-Assisted Organic Synthesis. From Single-Mode to Multimode Parallel Batch Reactors.," *Organic Process Research & Development*, vol. 7, pp. 707-716, 2003.
- [50] C. Kappe, "Controlled Microwave Heating in Modern Organic Synthesis," *Angew. Chem. Int. Ed.*, vol. 43, pp. 6250-6284, 2004.
- [51] Corradi, A.B., Bondioli, F., Focher, B., "Conventional and Microwave-Hydrothermal Synthesis of TiO₂ Nanopowders.," *J. Am. Ceram. Soc.*, vol. 88, no. 9, pp. 2639-2641, 2005.
- [52] Polshettiwar, V., Varma, R.S., *Aqueous Microwave Assisted Chemistry. Synthesis and Catalysis.*, Cambridge: The Royal Society of Chemistry, 2010.
- [53] Ryabochkina, P.A., Antoshkina, S.A., Vanetsev, A.S., Sildos, I., Gaitko, O.M., Kyashkin, V.M., Ushakov, S.N., Panov, A.A., Tabachkova, N.Yu., Nishchev, K.N.,

- “Synthesis, spectroscopic and luminescent properties of nanosized powder of yttrium phosphates doped with Er^{3+} ions,” *J. Nanopart. Res.*, vol. 16, pp. 2326-2334, 2014.
- [54] Caspers, H.H., Rast, H.E., Buchianan, R.A., “Intermediate Coupling Energy Levels for Nd^{3+} (4f3) in LaF_3 ,” *The Journal of Chemical Physics*, vol. 42, no. 9, pp. 3214-3217, 1965.
- [55] Mändar, H., Felsche, J., Mikli, V., Vajakas, T., “AXES1.9: new tools for estimation of crystallite size and shape by Williamson-Hall analysis,” *J. Appl. Crystallogr.*, vol. 32, pp. 345-350, 1999.
- [56] Wang, Y., Liu, Y., Xiao, Q., Zhu, H., Li, R., Chen, X., “ Eu^{3+} doped KYF_4 nanocrystals: synthesis, electronic structure, and optical properties,” *Nanoscale*, vol. 3, no. 8, pp. 3164-3169, 2011.
- [57] Li, C., Hou, Z., Zhang, C., Yang, P., Li, G., Xu, Z., Fan, Y., Lin, J., “Controlled Synthesis of Ln^{3+} ($\text{Ln}=\text{Tb}$, Eu , Dy) and V^{5+} Ion-Doped YPO_4 Nano-/Microstructures with Tunable Luminescent Colors,” *Chem. Mater.*, vol. 21, pp. 4598-4607, 2009.
- [58] Hikichi, Y., Sasaki, T., Murayama, K., Nomura, T., “Mechanochemical Changes of Weinschenkite-Type $\text{RPO}_4 \cdot 2\text{H}_2\text{O}$ ($\text{R}=\text{Dy}$, Y , Er , or Yb) by Grinding and Thermal Reactions of the Ground Specimens,” *J. Am. Ceram. Soc.*, vol. 72, no. 6, pp. 1073-1076, 1989.
- [59] Li, C., Xu, Z., Yang, D., Cheng, Z., Hou, Z., Ma, P., Lian, H., Lin, J., “Well-dispersed $\text{KRE}_3\text{F}_{10}$ ($\text{RE} = \text{Sm-Lu}$, Y) nanocrystals: solvothermal synthesis and luminescence properties,” *CrystEngComm.*, vol. 14, pp. 670-678, 2012.
- [60] Th. von Förster, “Squischenmolekulare Energiewanderung und Fluoreszenz,” *Ann. Phys.*, vol. 437, no. 2, pp. 55-75, 1948.
- [61] Orlovskii, Yu.V., Basiev, T.T., Samsonova, E.V., Glushkov, N.A., Eliseeva, S.V., Alimov, O.K., Orlovskii, A.Yu., Klimonsky, S.O., “Energy transfer probe for the characterization of luminescent photonic crystals morphology,” *J. Lumin.*, vol. 131, pp. 449-452, 2011.
- [62] Dexter, D.L., “A theory of Sensitized Luminescence in Solids,” *J. Chem. Phys.*, vol. 21, no. 5, pp. 836-850, 1953.
- [63] Agranovich, V.M., Galanin, M.D., *Electron Excitation Energy Transfer in Condensed Matter Series: Modern Problems in Condensed Matter Science*, vol. 3, New York: Elsevier North-Holland in Amsterdam, 1982.
- [64] Lecointre, A., Bessiere, A., Bos, A.J.J., Dorenbos, P., Viana, B., Jacquart, S., “Designing a Red Persistent Luminescence Phosphor: The Example of $\text{YPO}_4:\text{Pr}^{3+}, \text{Ln}^{3+}$ ($\text{Ln}=\text{Nd}$, Er , Ho , Dy),” *J. Phys. Chem. C*, vol. 115, pp. 4217-4227, 2011.
- [65] Ehrentraut, D., Sato, H., Kagamitani, Y., Sato, H., Yoshikawa, A., Fukuda, T., “Solvothermal growth of ZnO ,” *Progress in Crystal Growth and Characterization of Materials*, vol. 52, pp. 280-335, 2006.

Non-exclusive licence to reproduce thesis and make thesis public

Kerda Keevend

(author's name)

1. herewith grant the University of Tartu a free permit (non-exclusive licence) to:

1.1. reproduce, for the purpose of preservation and making available to the public, including for addition to the DSpace digital archives until expiry of the term of validity of the copyright, and

1.2. make available to the public via the university's web environment, including via the DSpace digital archives, as of **01.06.2017** until expiry of the term of validity of the copyright,

Microwave-hydrothermal synthesis of water-dispersible luminescent nanoparticles of yttrium phosphates and fluorides doped with Nd³⁺ ion

(title of thesis)

supervised by Alexander Vanetsev (Phd) and Yury Orlovskiy (Dr. hab, PhD)

(supervisor's name)

2. I am aware of the fact that the author retains these rights.

3. This is to certify that granting the non-exclusive licence does not infringe the intellectual property rights or rights arising from the Personal Data Protection Act.

Tartu, **25.05.2015**